Ocean Engineering 313 (2024) 119411

Contents lists available at ScienceDirect

Ocean Engineering

journal homepage: www.elsevier.com/locate/oceaneng

Research paper

Three-dimensional CFD-ALM-VOF modeling of hydrokinetic turbines in realistic open-channel conditions

Omar S. Mohamed [a], Pier Francesco Melani [a], Giuseppe Soraperra [b], Alessandra Brighenti [b], Giovanni Ferrara [a], Vittorino Betti [b], Leonardo Schippa [c], Massimo Guerrero [d], Francesco Balduzzi [a], Alessandro Bianchini [a,*]

[a] Department of Industrial Engineering, Università degli Studi di Firenze, Via di Santa Marta 3, 50139, Firenze, Italy
[b] HE-PowerGreen s.r.l., Via Solteri 74, 38121, Trento, Italy
[c] Department of Civil Engineering, Università degli Studi di Ferrara, Via Saragat 1, 44122, Ferrara, Italy
[d] Department of Civil, Chemical, Materials and Environmental Engineering, Università di Bologna, Viale del Risorgimento 2, 40136, Bologna, Italy

ARTICLE INFO

Keywords:
Actuator line model (ALM)
Darrieus
Vertical axis turbine (VAT)
Hydrokinetic turbines
Computational fluid dynamics (CFD)
Volume of fluid (VOF)

ABSTRACT

The potential of Darrieus-type Vertical Axis Turbines (VATs) in hydrokinetic applications, especially when deployed into arrays or clusters, has gained recognition in the field of distributed energy production. Due to the complex unsteady hydrodynamics of these turbines and the different flow scales involved, numerical studies to date have often focused on one system component only (turbine or channel). This study presents an integrate, accurate, but computationally feasible simulation approach applied to an array of VATs in a free-surface channel. The turbines are modelled using the Actuator Line Method (ALM), while the water free surface is modelled using the Volume of Fluid (VOF) approach, both included within the RANS solver of Ansys Fluent. A sensitivity analysis is conducted on the most appropriate model settings, followed by a validation campaign with field data that showed good agreement between experiments and simulations. Results point out the significance of the two-way interactions between the turbines and the channel, emphasizing the impact of the variation in water level and inflow velocity on the efficiency assessment of hydrokinetic turbines. The study also exploits the current 3D model to get a better understanding of the interaction effects between closely spaced turbines, and their influence on the power augmentation mechanisms in an array of turbines, which were so far mainly analyzed only with 2D approaches. Finally, the hydraulic impact on the channel is discussed, highlighting the effects and limitations of clustering hydrokinetic arrays in a confined channel.

1. Introduction

In conventional hydroelectric power generation, potential energy from water flow is harnessed as it falls from a considerable height. The energy produced in this process relies on two factors: the flow rate and the head of water. However, despite its superior efficiency over other renewable energy resources, this method is dependent on the presence of suitable morphological characteristics of the territory and often limited by economic, environmental, and ecological concerns (Yadav et al., 2023). Alternatively, interest is recently arising towards Hydrokinetic Turbines (HKTs), which are used to capture the kinetic energy from water streams in small channels and artificial water networks. Rated power outputs are generally small, but these systems can work well in combination with other renewables in the perspective of a distributed generation, are easy to regulate and have negligible impact on the surrounding environment.

Similarly to wind turbines, HKTs can be categorized based on the orientation of the axis of rotation with respect to the incoming flow, i.e., Horizontal Axis Turbines (HATs) and Vertical Axis Turbines (VATs). Although less efficient than HATs (Niebuhr et al., 2019), VATs have the advantage of easier maintenance due to the possibility of placing the generator outside of the water. On top of that, deploying two or more VATs in close proximity can lead to increased overall power production compared to stand-alone turbines, both for Darrieus type (Zanforlin and

* Corresponding author.
E-mail addresses: omar.sherif@unifi.it (O.S. Mohamed), pierfrancesco.melani@unifi.it (P.F. Melani), gsoraperra@he-powergreen.it (G. Soraperra), amministrazione@he-powergreen.it (A. Brighenti), giovanni.ferrara@unifi.it (G. Ferrara), studiobettievialli@gmail.com (V. Betti), leonardo.schippa@unife.it (L. Schippa), massimo.guerrero@unibo.it (M. Guerrero), francesco.balduzzi@unifi.it (F. Balduzzi), alessandro.bianchini@unifi.it (A. Bianchini).

https://doi.org/10.1016/j.oceaneng.2024.119411
Received 19 July 2024; Received in revised form 11 September 2024; Accepted 30 September 2024
Available online 9 October 2024

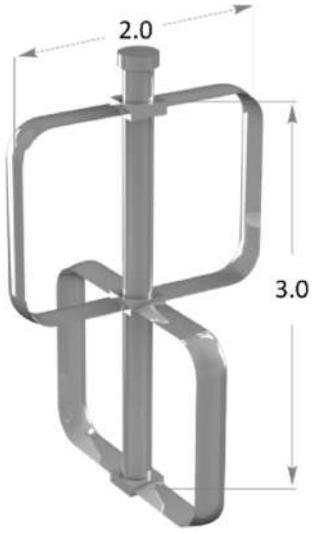

Fig. 1. a) schematic representation of the turbine model and b) blade profile.

Table 1
Geometrical characteristics of the test case turbine.

Dimension	Value
Number of blades [-]	2
Diameter, D [m]	2
Turbine height. H [m]	3

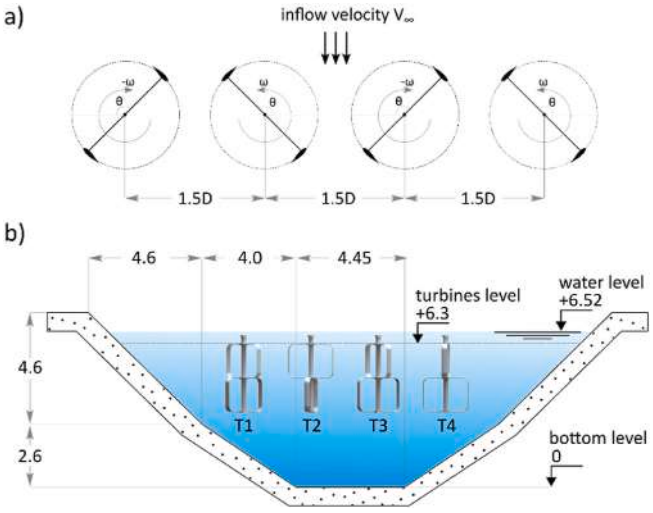

Fig. 2. Biffis channel cross section and dimensions in meters.

Table 2
Test operating conditions.

Parameter	Value
Tip-speed ratio [-]	2.09–3.15
Work fluid [-]	water
Inflow speed, V_∞ [m/s]	1.6
Inflow turbulence intensity [%]	0.24
Chord-based Reynolds number range, Re_c [-]	≈420k – 1,600k

Nishino, 2016; Mohamed et al., 2019, 2023a) and Savonius type (Nag and Sarkar, 2021; Chen et al., 2022). (Zanforlin and Nishino, 2016), (Mohamed et al., 2019), (Mohamed et al., 2023a). (Nag and Sarkar, 2021)., (Chen et al., 2022)

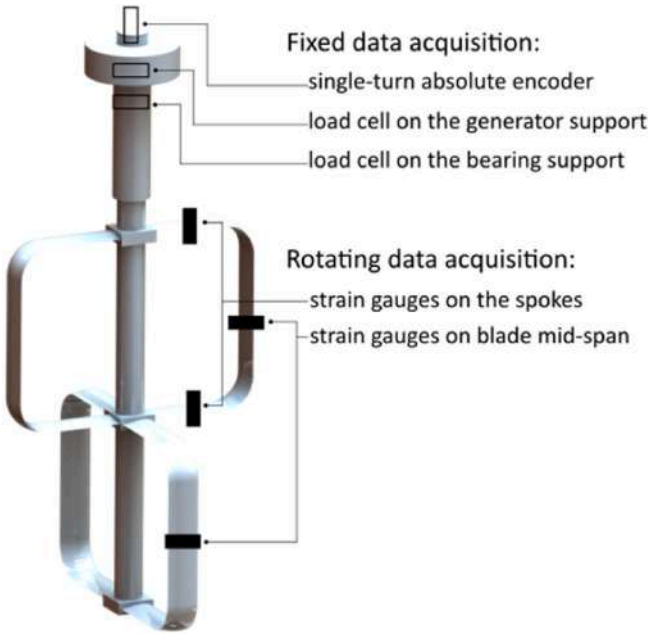

Fig. 3. Locations of the sensors used during the performance measurements experimental campaign.

The achievable power augmentation thanks to array effects, nonetheless, is limited by the interaction between HKTs and the channel hydraulic system. Several studies have investigated this phenomenon in subcritical flows conditions. For instance, an experimental campaign has been carried out by Mayers and Bahaj (Myers and Bahaj, 2007) on a HKT operating in a recirculating channel. They observed a rise in water level relative to the free surface near the upstream due to blockage, a decrease near the downstream due to energy extraction, followed by a subsequent rebound in the far downstream due to wake recovery. These observations have been confirmed in other studies (e.g. (Kirke, 2019; Chaulagain et al., 2023),). (Kirke, 2019)., (Chaulagain et al., 2023)

The prediction of this turbine-channel interaction is, however, a challenging task, due to the intrinsically unsteady operation, massively involving stall and creation of vortical structures, that characterizes Darrieus turbines. Several analytical models based on the Blade Element Momentum (BEM) were recently introduced to describe the performance of an array of Darrieus HKTs, often relying on the Double Multiple Streamtube (DMST) approach. Nishino and Willden (2012) developed an analytical model based on the actuator disk theory, to which they thereafter added a sub-model to account for the effect of array-scale flow expansion (Nishino and Willden, 2013). Their model was able to describe general trends related to the relation between the number of turbines within the array and the limit of power extraction per turbine. Draper and Nishino (2014) further developed the model to study centered and staggered arrays. Cacciali et al., 2022, 2023a developed a DMST-based model that iteratively updates the inflow upstream to a Darrieus HKT based on the downstream conditions in a free surface channel environment. In general, these analytical models are usually used as a rapid tool for the preliminary design, given that the BEM-based models in VATs are inherently incapable of predicting second-order phenomena. i.e., vortex shedding and blade-wake interaction, as well as three-dimensional effects. (Cacciali et al., 2022)., (Cacciali et al., 2023a)

On the other hand, Computational Fluid Dynamics (CFD) simulations come as a reliable tool for predicting such complex phenomena, however, with far more computational effort compared with analytical models. During the last couple of decades, CFD has played an important role in understanding the aero/hydrodynamic characteristics of these machines (Mohamed et al., 2021, 2023a; Melani et al., 2020). It is

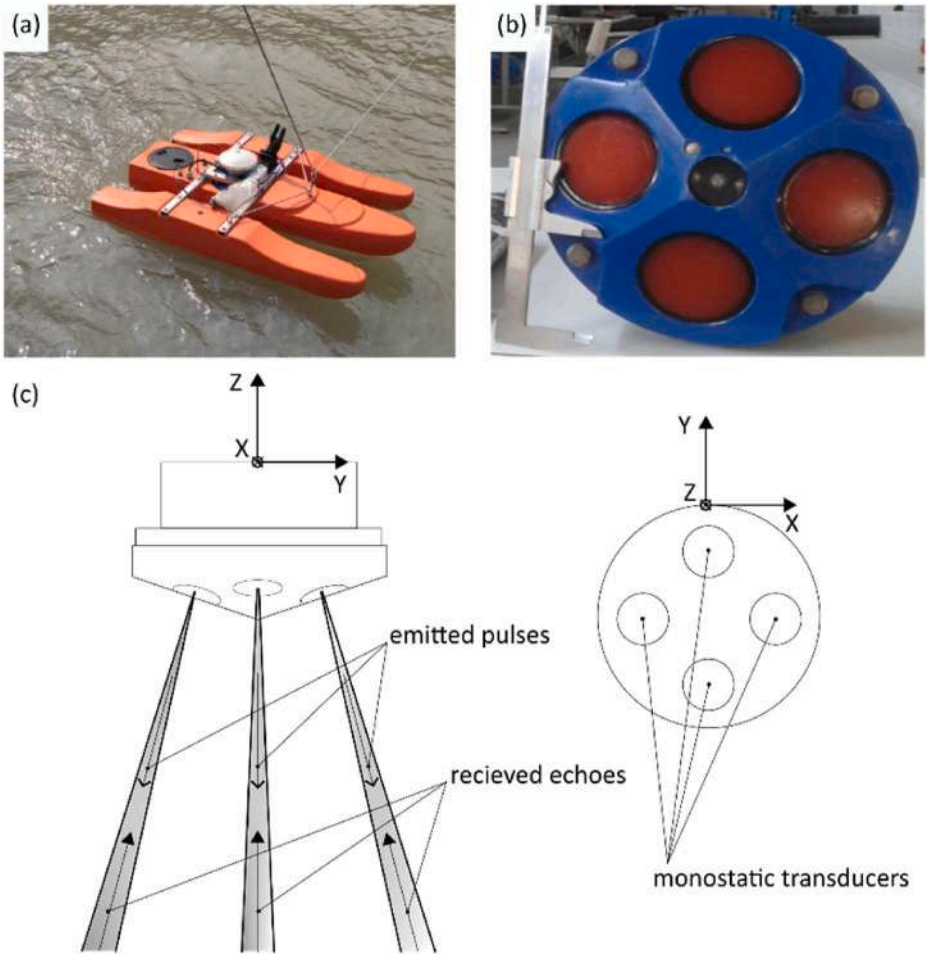

Fig. 4. (a) The boat used to mount the ADCP, b) ADCP instrument, c) schematic representation of the ADCP working concept.

important to note that due to constrains related to computational cost, most of these studies employed a two-dimensional approach without considering the effect of the two-way interactions between the turbines and the channel. However, these interactions in a three-dimensional domain need to be taken in consideration in several important aspects connected to the overall behaviour of these machines. For example, Nishi et al. (2017) and, recently, Yosry et al. (2023) conduced blade-resolved CFD studies for Darrieus HKT using Volume of Fluid (VOF) to model the free water surface, and they both showed that a single-phase simulation of a hydrokinetic turbine results in significantly overestimated power output compared to a two-phase simulation. (Mohamed et al., 2023a), (Melani et al., 2020)., (Mohamed et al., 2021)

Hybrid simulation techniques, such as the Actuator Line Method (ALM) were recently proposed to substitute the conventional blade-resolved CFD in the simulations of Darrieus turbines (Melani et al., 2021a). In ALM, blade loads are estimated based on the sampled local inflow conditions using tabulated polar data as in engineering methods. These forces are then inserted into the computational grid as equivalent volume momentum sources. A CFD-based method is then used to solve the flow field. Since the geometry of the turbine blade is not explicitly resolved, but instead modelled using a lumped-parameter representation, the overall grid density of the simulation is significantly reduced, resulting in a corresponding decrease in computational cost.

The VOF method, as detailed in (Yosry et al., 2023; Gauvin-Tremblay and Dumas, 2020), when coupled with blade-resolved CFD, has proven effective for simulating the free water surface in hydrokinetic turbines, addressing crucial aspects of free-surface modeling. Building on this foundation and the authors' previous research, particularly regarding the development and refinement of an ALM tool, tailored to VATs (Melani et al., 2021a) both isolated (Mohamed et al., 2022) and in array configurations (Mohamed et al., 2023b), the present study introduces a novel framework that bridges the gap between BEM-based models and blade-resolved CFD. This framework is specifically designed for the simulation of hydrokinetic turbine arrays under realistic channel flow conditions. It couples the ALM tool with a two-phase, three-dimensional model of a realistic water channel that employs the VOF approach to accurately capture free-surface effects (Gauvin-Tremblay and Dumas, 2020).

A systematic sensitivity analysis to optimize the numerical model and understand its limitations is performed, followed by a validation campaign against unique experimental field measurements on an industrial 4-rotors array operating in a channel in Italy (Guerrero et al., 2023). This validation involves performance, water level, and flow field data and is considered to be a major point of strength of the study. The load results of the array are then analyzed, followed by an assessment of the corresponding power augmentation mechanism. The results are compared with 2D findings to gain a deeper understanding of how closely spaced deployment can enhance the power coefficient in a confined channel within a realistic three-dimensional context. Finally, the impact of the array deployment on the channel is investigated, highlighting the potential and drawbacks of such turbine installations.

The paper is organized as follows. In Section 2, the hydrokinetic turbine model featured in this study is presented along with the configurations studied for the array configuration in addition to the geometrical and hydraulic characteristics of the channel. Section 3 details the methodology employed in the present study, including the ALM

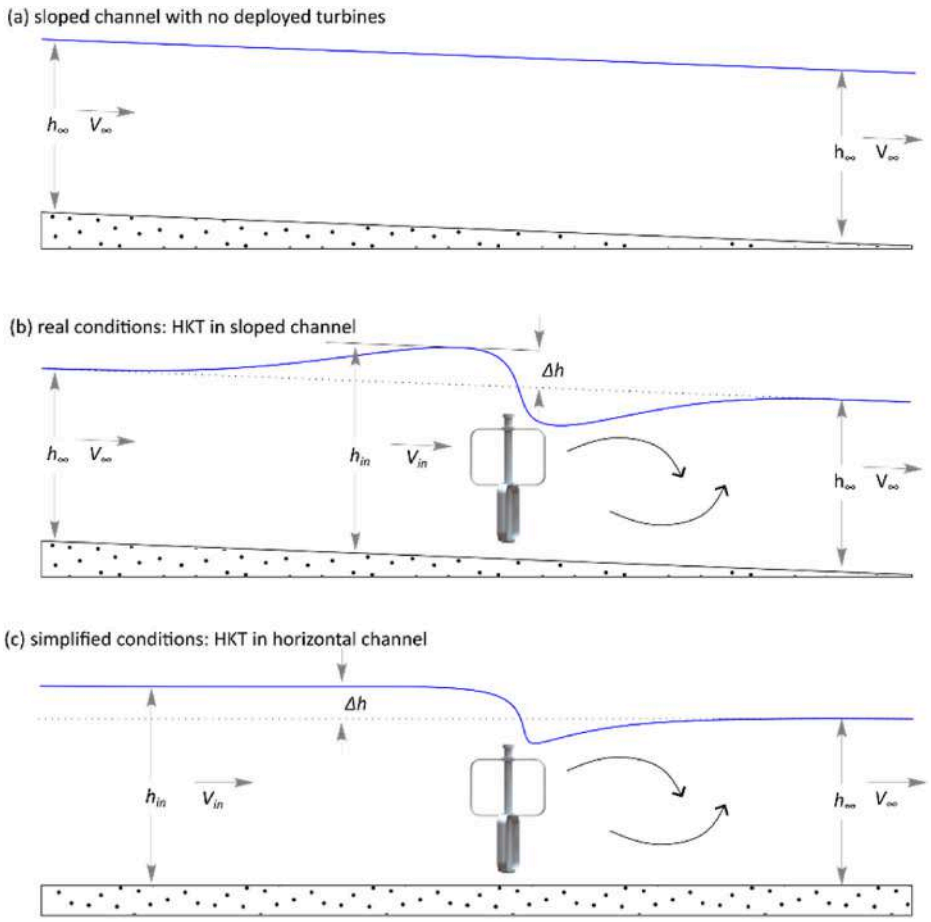

Fig. 5. Schematic representations of (a) sloped bed channel without turbine, (b) with turbine, and (c) horizontal bed channel with a turbine.

algorithm, the CFD settings, and the experimental setup and measurement techniques. Section 4 reports the results of the numerical sensitivity analysis carried out and concludes the final model. Section 5 shows the validation results and reports some critical analysis on the turbine performance for both stand-alone turbine and an array of four turbines. Finally, Section 6 presents the conclusions of the study and some handouts for future developments.

2. Test cases

2.1. Hydrokinetic turbine model

The turbine model (see Fig. 1) used in the present study is an industrial two-bladed H-Darrieus hydrokinetic turbine with a diameter of 2 meters (see Table 1), designed in collaboration with the industrial partner HE-Powergreen in a previous work (Balduzzi et al., 2021). This turbine is segmented at its midspan (1.5 meters), allowing the upper and lower rotors to be positioned perpendicular to each other, with a 90° azimuthal shift. This configuration was implemented to address mechanical balance issues and reduce the output torque ripple. The blades' design uses a proprietary airfoil derived from the DU-06-W-200 by optimizing the thickness distribution and accounting for flow curvature effects (Rainbird et al., 2015). Similar turbine concepts have been employed in various prior studies for different purposes (Mohamed et al., 2022, 2023b; Melani et al., 2021b) at which for all of them, the present ALM code was used, and it showed very good results compared to blade-resolved CFD. (Mohamed et al., 2022), (Mohamed et al., 2023b)., (Melani et al., 2021b)

2.2. Channel description

In the current study, both stand-alone turbine and array of four turbines are evaluated. In the case of turbine array, a consistent center-to-center distance of 1.5 times the rotor diameter (1.5D) is used, with the rotational orientation scheme shown in Fig. 2-a. The operational characteristics of the turbines can be found in Table 2.

Fig. 2-b shows the channel used in the present study. It is part of the Biffis artificial channel with a double trapezoidal shape located near the city of Trento, Italy (Il Canale Biffis). The channel section has a width of approximately 21.65 m, with a wetted width of about 20.2 m, corresponding to a volume flow rate of 124 m^3/s. The bottom width measures approximately 4.45 m. The maximum height from the bottom to the top is 7.2 m, with a wet height of 6.52 m. More details on the channel are presented in previous work by Cacciali et al. (2023b). In the real channel, the section remains with the same shape with slight variations in the dimensions upstream and downstream the presented section at which the turbine array is installed.

3. Methodology

3.1. Experimental setup

In this section, the setup of the experimental campaign is discussed, including the measurement techniques and the uncertainties associated with the data acquisition and postprocessing.

The performance of the turbines was measured using different types of sensors, some stationary while others rotate, as illustrated in Fig. 3. To avoid signal transmission between fixed and rotating parts using slip rings or wireless transmitters, which are not well-suited for the specific

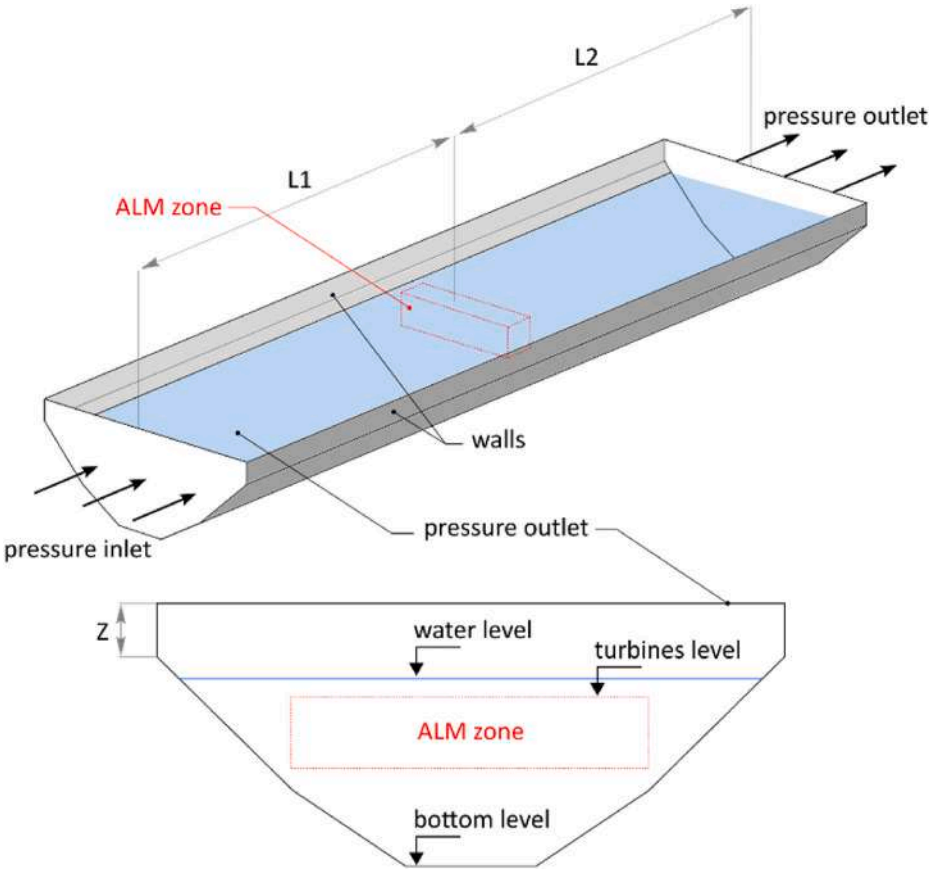

Fig. 6. Schematic representation of the channel CFD domain and boundary conditions.

case at hand, a dedicated data acquisition subsystem was mounted at the upper end of the shaft. This box rotates and is integral with the shaft itself, requiring the shaft to be extended and equipped with an appropriate connection system. The rotating data acquisition subsystem collects and saves signals from sensors installed on the moving parts, which are then exported via physical access, as real-time measurements are not necessary. In parallel with the rotating subsystem, a stationary subsystem was installed to collect signals from transducers attached to the fixed system, synchronized with the former at startup. The residual synchronization error between the rotating and fixed systems is estimated to be approximately ≈10 milliseconds.

The sensors connected to the rotating subsystem comprise four strain gauges. Two of these gauges are installed at the midspan of one of the blades on the upper and lower rotors, while the other two are mounted on the spokes connecting the blades of the upper rotor to the shaft. These sensors are responsible for measuring the bending moment with a residual accuracy of about ±2%. On the other hand, the fixed subsystem is connected to load cells on the generator support, measuring the total forces acting on the turbine in the X and Y directions with a residual accuracy of ±0.5%. Additionally, a single-turn absolute encoder is mounted on the top of the shaft to compute the instantaneous angular position of the blades, with a residual accuracy of ±1%.

For velocity measurements, the Acoustic Doppler Current Profiler (ADCP) was utilized. In the present study, the ADCP was mounted on a boat, as shown in Fig. 4-a, with the measurement profile oriented vertically from the free surface to the channel bottom. The instrument used is the WorkHorse-1200kHz by Teledyne-RDI, depicted in Fig. 4-b, which provides a three-components velocity profile with a resolution of 0.25 meters from approximately 0.6 m below the free surface to about 94% of the depth, with maximum depths reaching around 20 m. The velocity standard deviation was limited to less than 1 cm/s by appropriate instrumental settings (Guerrero et al., 2023) for the single estimation which entailed about 1-Hz acquisition frequency.

As schematically represented in Fig. 4-c, the ADCP consists of four monostatic cylindrical pistons which alternate emission and reception functionalities (namely, monostatic transducers) oriented in a divergent manner, projecting and receiving broadband signals into four acoustic beams from the free surface toward the bottom. The areas not measured near the interfaces mainly depend on the time between emission and reception (i.e., the ringing effect) close to the instrument and the reflection of the side lobes characterizing the beam pattern of cylindrical pistons. This latter limitation is particularly relevant in conditions of channel sloping sides, the profile is limited by the external region of beam pattern (i.e., side lobe) that is reflected by sloping sides more superficially than the beam main axis pointing towards the bottom. The pulses emitted along the four beams are scattered at different depths and then received at successive intervals, determining the vertical resolution of the profile.

To measure the water level variation, a set of water level sensors has been set up at various points along a channel. At each point, there are two types of sensors: IFM – UIT501, which is an ultrasonic level sensor with programmable digital threshold, and Vega – Vegaplus 62, a radar level sensor. Over a period of 48 h, data was continuously collected while four turbines were operational. The process of measuring water levels involves several steps. Initially, raw data is gathered at a rate of 1 Hz from the ultrasonic level sensor at different points. However, a residual offset is present between the points, likely due to slight variations in embankment height and sensitivity to sensor temperature. To mitigate this, a tuning process is implemented, introducing an additional offset to align the average signals across all points along the channel. The corrected water level value is derived using the reference level measured by the Vega radar level sensor to adjust the data across all points. This comprehensive procedure ensures precise water level measurements across the various points, despite inherent challenges and

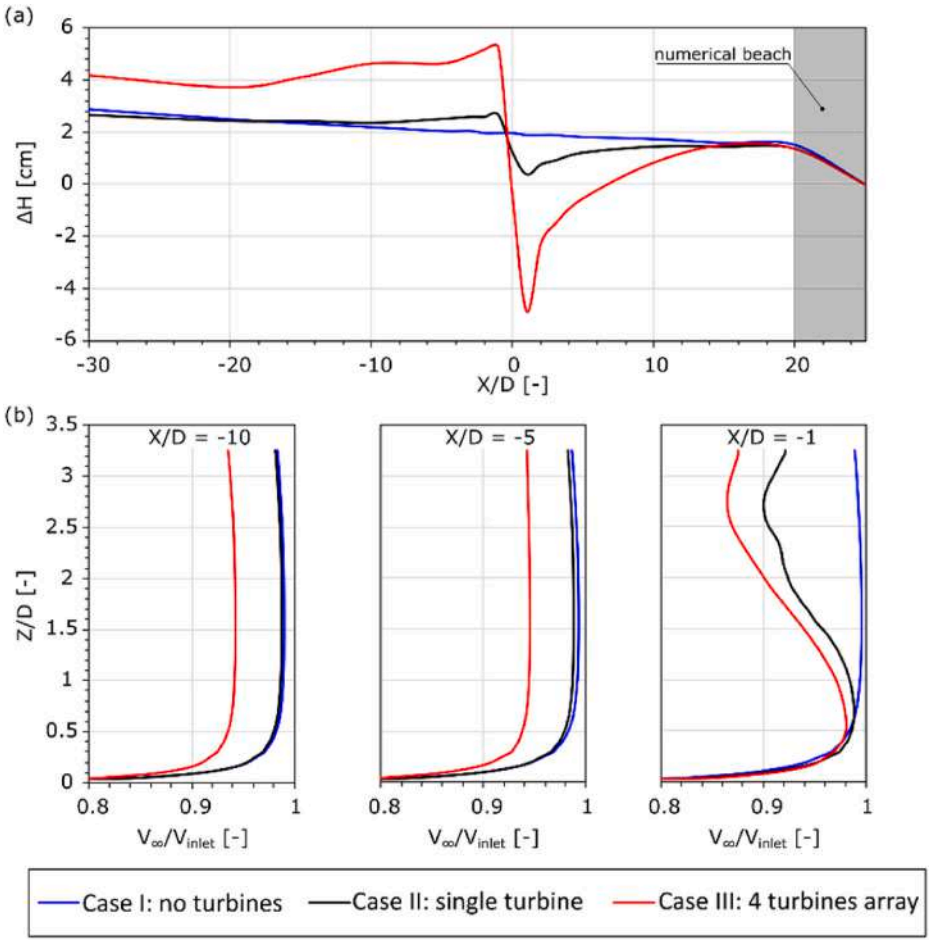

Fig. 7. a) water level variation and b) dimensionless velocity profiles for the channel with no turbines, stand-alone turbine, four-turbine array.

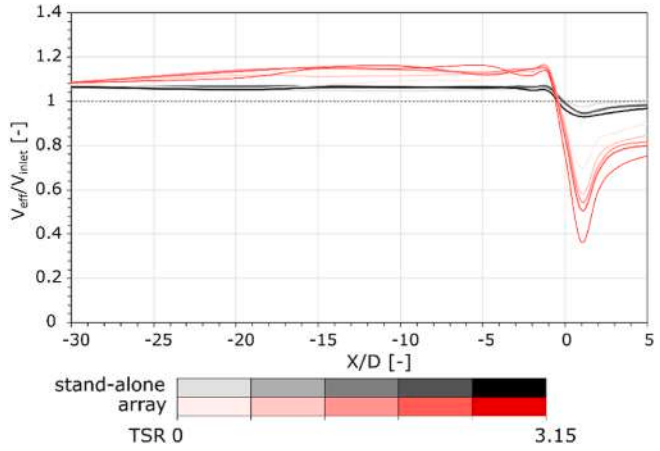

Fig. 8. Variation in the effective velocity V_{eff}/V_{inlet} for the stand-alone turbine and the array at different TSRs.

differences in sensor readings.

3.2. Numerical model

All CFD simulations were conducted using Ansys Fluent 23 R1. This section outlines the key characteristics of the CFD model used, along with a brief overview of the algorithm in the present ALM formulation.

Table 3
Models used in the domain independency test.

Name	L1/D	L2/D	Z/D
Effect of height Z			
D1.1	10	25	1
D1.2	10	25	2
Effect of downwind distance L2			
D2.1	10	25	1
D2.2	10	30	1
Effect of upstream distance L1			
D3.1	10	25	1
D3.2	20	25	1
D3.3	30	25	1
D3.4	40	25	1

3.2.1. Actuator Line Method (ALM)

The ALM (Sørensen and Shen, 2002) has recently become a widely used computational tool for simulating wind turbines. The ALM algorithm positions actuator lines representing turbine blades within the computational grid, samples the local Reynolds number and angle of attack for the blade, and utilizes available polar data, along with additional sub-models, to compute aerodynamic forces. These forces are then applied as momentum source terms within the RANS solver to integrate them into the computational domain. In this study, the ALM tool used is a version specifically developed and customized for VATs by some of the authors (Melani et al., 2021a). It is important to note that the current ALM code was specifically designed to be compatible with the Ansys Fluent UDF environment. However, open-source alternatives for ALM in VATs, such as the one developed by Bachant et al. (2018), are also

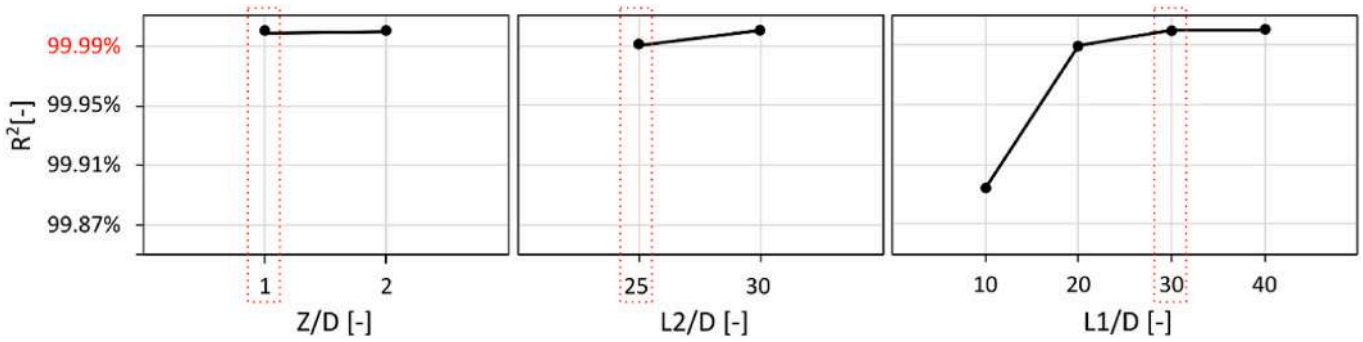

Fig. 9. Domain size sensitivity analysis results: a) effect of height Z, b) downstream distance L2, c) upstream distance L1.

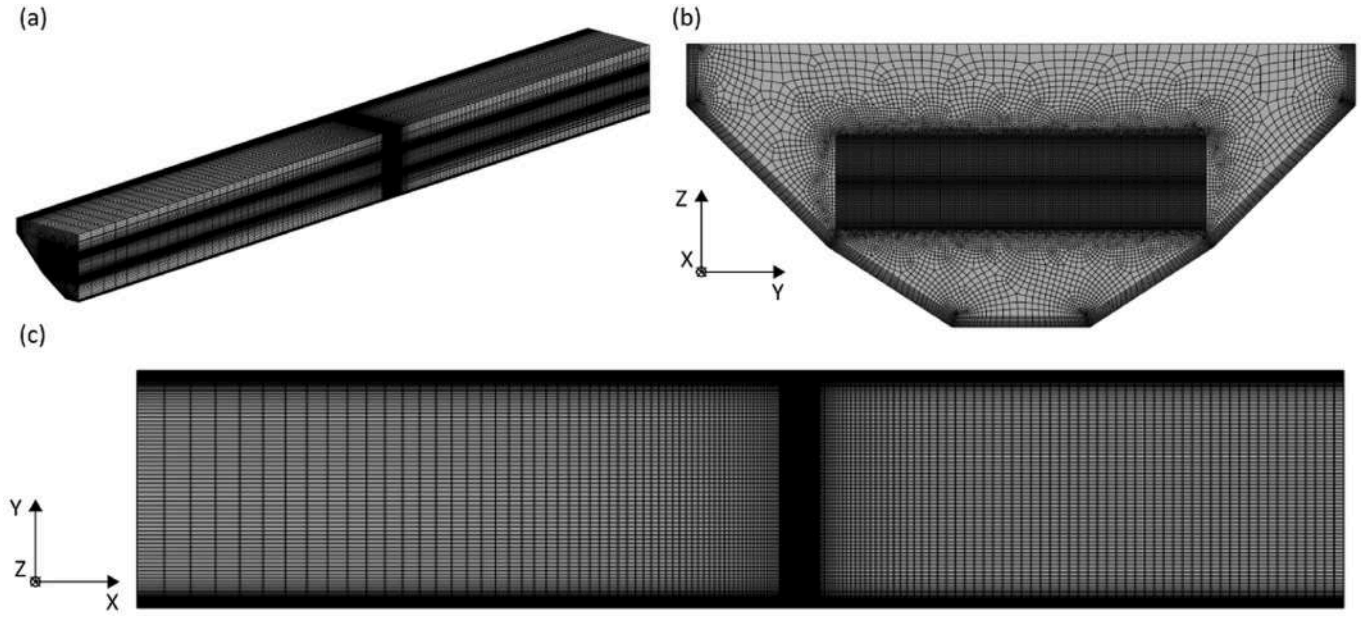

Fig. 10. a) isometric sectional view of the mesh b) sectional front view of the ALM region within the channel c) channel top view.

Table 4
Grids used in the mesh independency test.

Name	#divisions - L1	#divisions - L2	Δh	air-water interface	# elements
M1	60	50	β	n	5,317,444
M2	60	50	β/2	n	6,625,040
M2B	60	50	β/2	y	10,824,580
M3	90	75	β/2	n	8,393,344

available and could be readily used for similar analyses, provided that the coupling with a VOF model is possible. Some unique features of the present code include:

- **Sampling of the local flow field:** The LineAverage method, originally proposed by Jost et al. (2018) for horizontal-axis wind turbines and validated by the authors (Melani et al., 2020; Mohamed et al., 2021) for vertical-axis turbines, estimates the blade AoA from the local flow field. It calculates the undisturbed velocity by averaging the velocity field along a circular line with a radius of r = 1c, consisting of 80 equally spaced points and centered on the quarter-chord of the airfoil. Additionally, a low-pass filter is applied, implemented using a Cubic Spline Smoothing (CSS) algorithm (de Boor, 1978) following the procedure outlined in (Melani et al., 2021c). (Melani et al., 2020), (Mohamed et al., 2021)
- **Polar data:** The quality of the predictions made by the ALM relies heavily on the quality of the polar data it utilizes. This aspect holds particular importance for small Darrieus rotors, as indicated in a prior study conducted by some of the authors (Melani et al., 2021c). In such cases, where low Reynolds numbers and the influence of laminar separation bubbles on airfoil aerodynamics are accentuated, the reliance on high-quality polar data becomes more pronounced. It is noteworthy that the tabulated polar data referenced in the present work pertains to the airfoil that has been virtually transformed, as detailed in (Rainbird et al., 2015). The aerodynamic coefficients before stall were obtained through two-dimensional blade resolved CFD using k-ω SST with Gamma transport equation to solve transition (Menter et al., 2015). Moreover, the range of the polar data was expanded to encompass the deep stall region, up to an angle of attack of ±180°, employing the Viterna-Corrigan model (Viterna and Janetzke, 1982), in accordance with the recommendation by Bianchini et al. (Marten et al., 2016) for applications involving Darrieus turbines;
- **Forces computation and dynamic stall model:** The present code employs Berg dynamic stall model (Massé, 1981) to account for the unsteady flow effects on blade loads, as elaborated in (Melani et al., 2021c). This model introduces a delay in the measured angle of attack, which varies proportionally with the flow reduced frequency, thereby incorporating dynamic effects into the solution. Lift and drag coefficients are determined through linear interpolation between

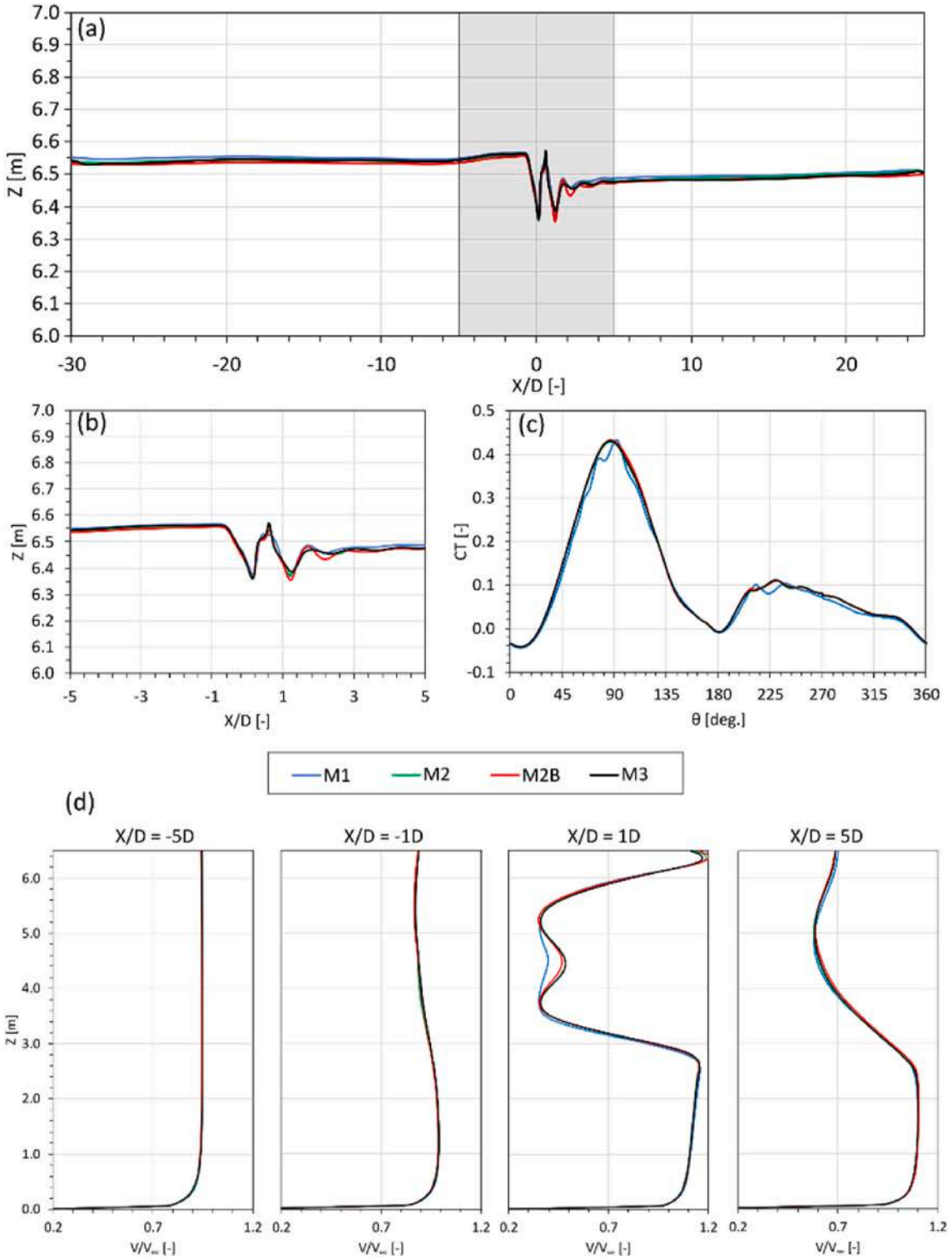

Fig. 11. Results of the mesh independency test a) water level along the full channel with a zoomed area of b) water level near the turbines c) instantaneous torque coefficient d) dimensionless velocity profiles.

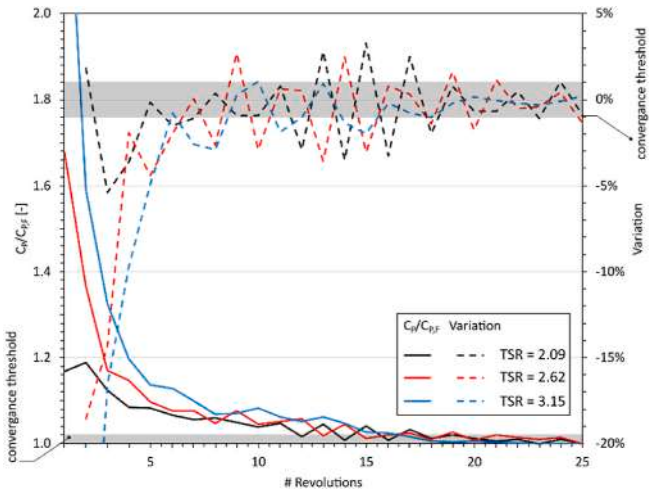

Fig. 12. Convergence histories based on the power coefficient at TSRs 2.09, 2.62, and 3.15.

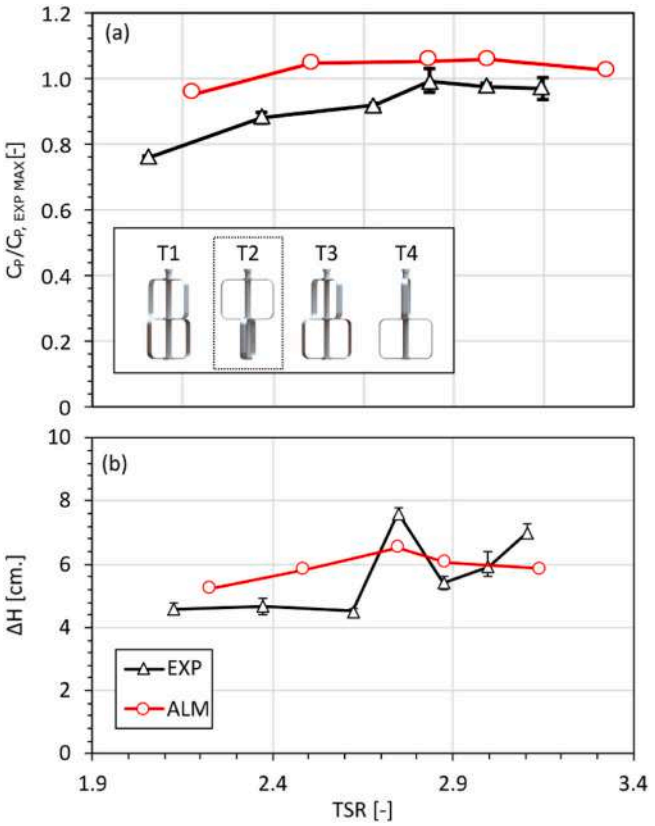

Fig. 13. Comparison between average power coefficient obtained numerically and that of the experimental data normalized over the maximum experimental C_P for turbine 2 in the four-turbine array.

static and dynamic coefficients, with a weight given by the constant A_M, here set to 6. Added mass terms were also included by modifying the normal and tangential forces coefficients, $C_{N,\ AM}$ and $C_{T,\ AM}$, according to Eqs. 1) and (2):

$$C_{N,AM} = -\pi \cdot c \cdot \frac{dV_N}{dt} \frac{1}{8\ V_{rel}{}^2} \tag{1}$$

$$C_{T,AM} = \pi \cdot c \cdot \frac{d\alpha}{dt} V_N \frac{1}{8\ V_{rel}{}^2} \tag{2}$$

with c the chord length, V_{rel} the relative velocity, and V_N the normal velocity. dV_N/dt and $d\alpha/dt$ are the rate of change of the normal velocity and angle of attack, respectively.

- **Tip effects correction:** The Dağ-Sørensen (DS) correction (Sørensen et al., 2014) is applied in the present work to account for tip effects. The application of this correction to the ALM is based on the similarities between the effects on the flow field caused by the ALM's isotropic Gaussian smearing function and those of a Lamb-Oseen vortex, with a viscous radius equivalent to the kernel width β. Melani et al. (2022) demonstrated and successfully applied the correction to a Darrieus turbine, showing reasonably accurate results. It is noteworthy that the current tip effects correction formulation does not encompass the contribution of the vorticity shed in the wake, unlike the original work (Sørensen et al., 2014). Additionally, the application of this correction to blades with curved ends, such as the one under investigation, might introduce some uncertainties. Although the authors have recently made efforts to tune the ALM for simulating tip effects (Melani et al., 2024a, 2024b), their effects on rotating blades are more complex and warrant a separate investigation. (Melani et al., 2024a), (Melani et al., 2024b)

Additional information about the present ALM code formulation can be found in (Melani et al., 2021a).

3.2.2. CFD setup

In order to build a CFD model that is capable of simulating the physical parameters of interest, careful consideration must be taken into account while putting the assumptions that should reduce the computational cost. As illustrated in Fig. 5-a, for a sloped uniform channel, i.e., constant cross-section, a steady equilibrium must be satisfied between the gravity force associated to the slope of the channel and the friction on its walls. Thus, the water depth h_∞ and flow velocity V_∞ at the inlet remain constant as long as the uniformity and steadiness constraints are maintained. Deploying HKTs into that system (Fig. 5-b) would perturb the water level, altering in turn the stream velocity upstream of the turbine. Based on the energy balance, the blockage effect due to the turbine will cause the water level to increase upstream to a maximum height of h_{in} while decreasing the flow velocity to V_{in}. Downstream of the turbine, the water level decreases again, for then returning to its unperturbed value h_∞ far downstream. This is also known as "depth recuperation". The upstream rise in water level corresponds to the drop in hydraulic head, $\Delta h = h_{in} - h_\infty$ that is a feasible assumption for negligible head dissipation.

Resolving such system using CFD would require extremely long domains, as reported by Gauvin-Tremblay and Dumas (Gauvin-Tremblay and Dumas, 2020). Alternatively, a simplified model can be created, in which the channel bed can be assumed horizontal ("*horizontal bed assumption*"), thus producing a water level profile like that illustrated at Fig. 5-c. In these conditions, the VOF (Hirt and Nichols, 1981) method allows the water level to vary based on the resolved flow field, fixing it at the outlet while allowing it to change at the inlet. The main drawback of this assumption is that it is not possible to compute distance required to reach the "depth recuperation". However, the estimation of the upstream rise, Δh, is still feasible.

Regarding the VOF method, it was employed to simulate the channel free surface, solving the flow fields of water and air through a single set of momentum equations while tracking the volume fraction of each fluid across the domain. This method operates on the principle that two or more fluids cannot compenetrate. It introduces the volume fraction of each fluid as a new variable for every computational cell. The volume fraction equation is then solved for the secondary phase, while that of the primary phase is computed so that the total volume fraction sum is unity (ANSYS FLUENT 12). A constant surface tension of 0.072 N/m was set to the water surface. Regarding the numerical discretization of the

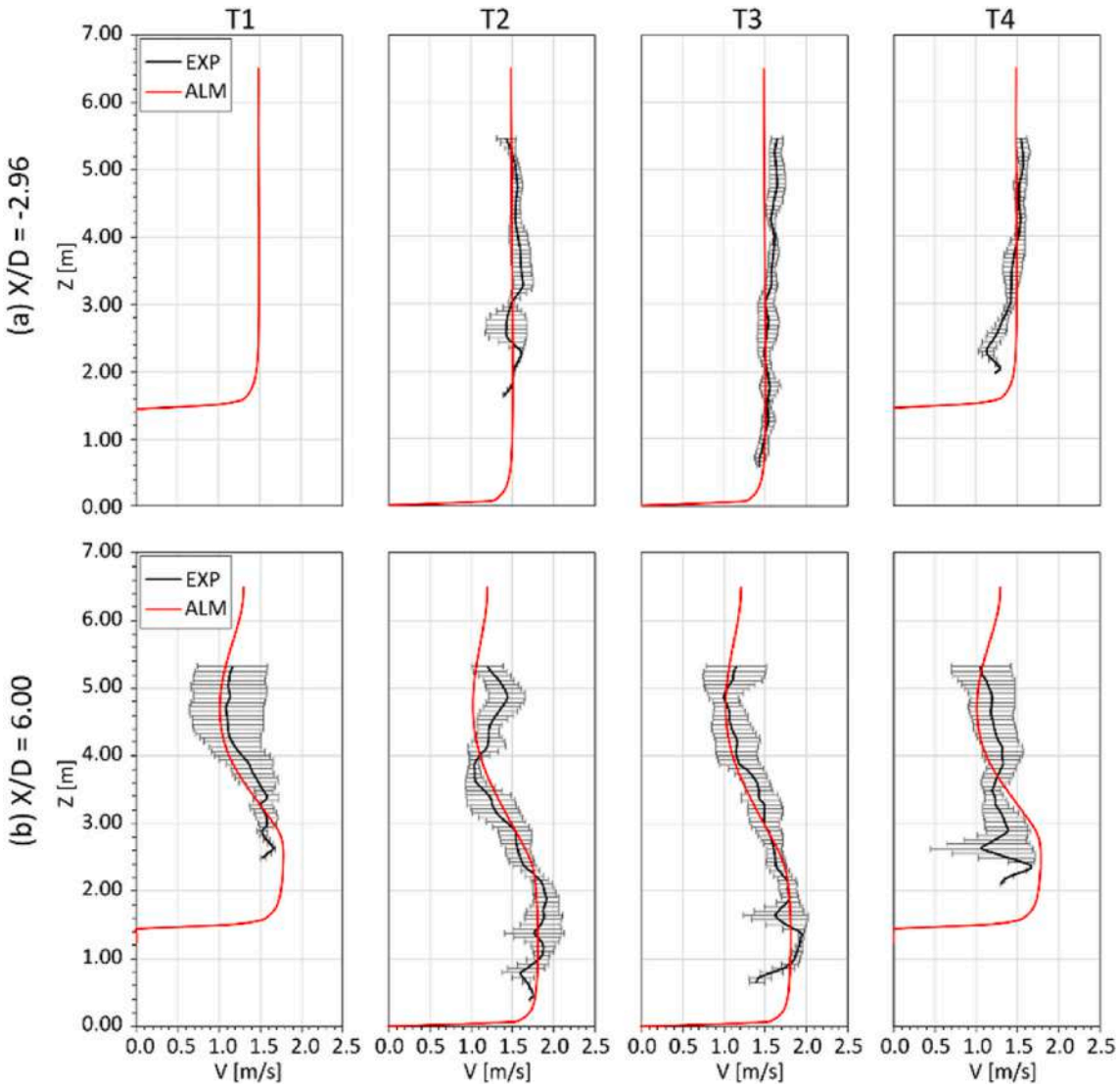

Fig. 14. Comparison between numerical model and experimental data velocity profiles for the four-turbine array upstream and downstream the turbines.

volume fraction, two different schemes were evaluated: compressive and modified High Resolution Interface Capturing (HRIC). However, both schemes predicted the same variations in the water level, so the default compressive scheme was used.

Three-dimensional simulations were performed using the unsteady Reynolds-Averaged Navier-Stokes (URANS) solver. The k-ω Shear Stress Transport (SST) model (Menter, 1993) was selected for the turbulence closure, renowned for its accuracy and stability in unsteady flow conditions (Balduzzi et al., 2016a). The pressure-based solution was employed using a coupled algorithm, and a second-order upwind scheme was utilized for the spatial discretization of all transport equations. The time difference employed a second-order implicit scheme. Additionally, based on previous experience on this type of simulations, the residuals for all variables were set to 10^{-5}, and 20 inner iterations were performed per time step, where the time step size Δt corresponds to $\Delta\theta = 1°$, based on the sensitivity analysis performed by Melani (Melani, 2018). Furthermore, other simulation details, including the domain and grid sizes were selected based on a dedicated sensitivity analysis that is presented in Section 4.

Fig. 6 shows the computational domain and boundary conditions of the present model. The domain includes the channel cross-section extruded in both upstream (*L1*) and downstream (*L2*) directions, as well as a volume of air of height Z on top of the water surface. Its dimensions were selected to ensure the consistency of the applied boundary conditions (see Section 4.2): i) pressure inlet at the inlet, with a prescribed velocity used to compute the dynamic component of pressure, treated as the total pressure prior to solving the flow field due to the absence of height differences, thanks to the horizontal bed assumption; ii) pressure outlet at the outlet of the channel and the top boundary; iii) no-slip condition at all channel walls. It is important to note that, for a simplified horizontal open channel model, the solution is initialized assuming a flat water surface, with constant velocity from inlet, then boundary conditions set at the inlet change as the simulation run, due to the variation in the energy gradient level along the channel, causing the pressure field to change thanks to the flow interactions with the turbines and the channel walls, which in turn alters the velocity and water level upstream compared to its prescribed values at the pressure inlet. Finally, although no waves have been imposed at the inlet, a numerical beach is applied before the outlet to create an artificial wave-damping procedure to avoid flow reversal.

4. CFD sensitivity analysis

This section presents the main results of the sensitivity analysis carried out on the proposed CFD model, initially highlighting the significance of the assumption of having a horizontal bed instead of sloped

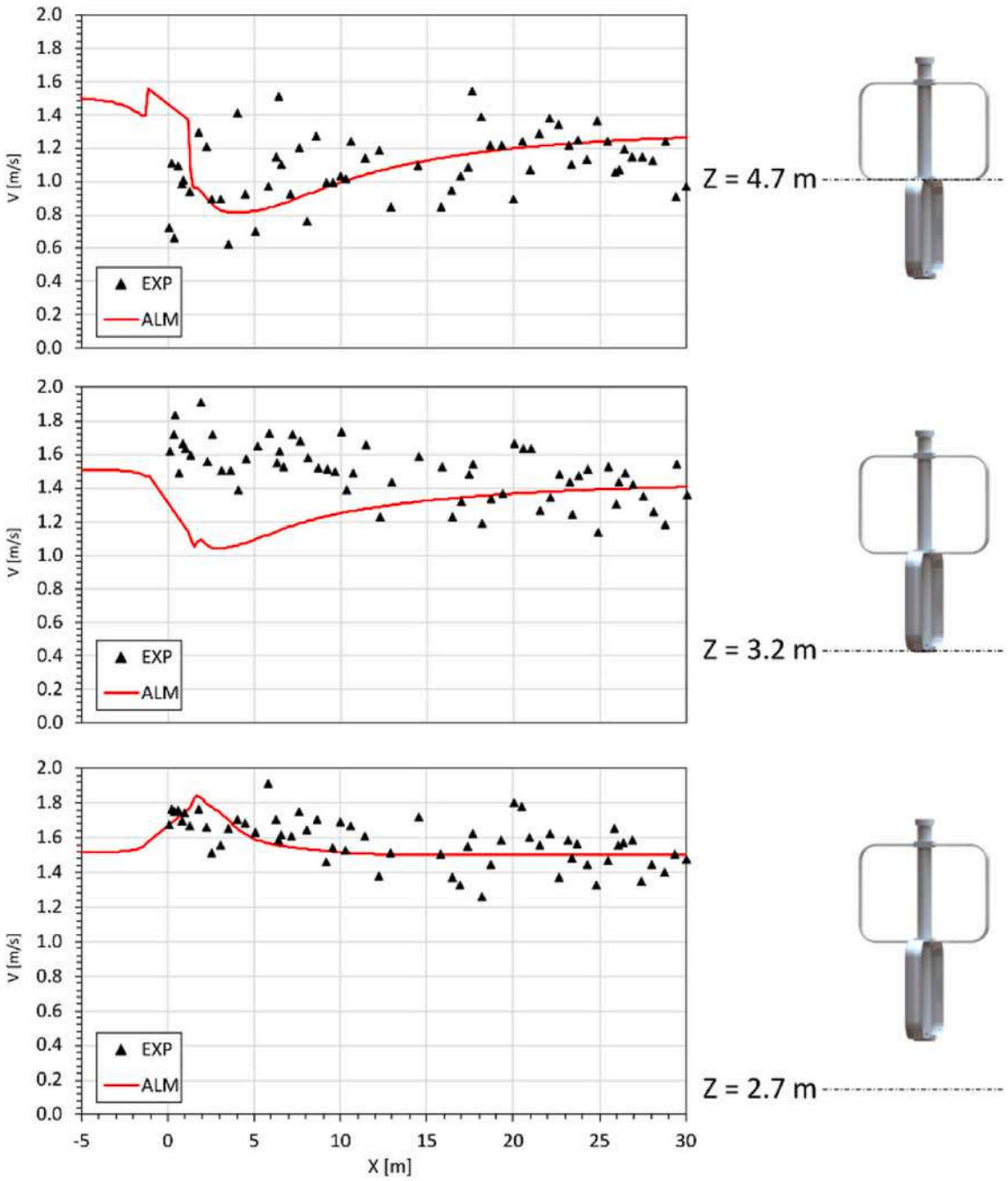

Fig. 15. Comparison between numerical model and experimental measurements of velocity in the wake of T2 centre for a four-turbine array at different Z levels.

one (see Section 4.1), then moving to the numerical independence analysis for the domain (see Section 4.2) and mesh sizing (see Section 4.3).

4.1. Testing the horizontal bed assumption

To assess the horizontal bed assumption, three different cases were simulated: Case I, where no turbines are operating inside the channel, Case II with a single operating turbine located at the channel center, and Case III, where an array of four turbines is operating, with the layout mentioned previously in Fig. 2-a. Fig. 7 shows a comparison between the water level variation in terms of ΔH and the velocity profile at different upstream distances for the three cases. It is important to highlight that the water level was computed for several 2D cross-sections across the domain length, thus accounting for the three-dimensional nature of the channel. As can be observed, the water level in Case I shows a smooth slope from inlet to outlet with no perturbations throughout the domain; given that the channel is assumed to have a horizontal bed, this is due to the friction losses. In Case II, the water level follows that of Case I far upstream, while the effect of blockage due to the interaction between the water stream resource and the operating turbine can be observed at $X/D < -10$. On the other hand, for Case III, the blockage effect is much stronger than that in Case II due to the presence of four turbines, which results in a significant upstream rise that is propagated up to the inlet. For all the cases, the impact of the numerical beach set at outlet is clearly visible, damping the induced waves at outlet to prevent backward flows.

The efficiency or the power coefficient C_P of the turbines is computed through dividing the power generated P over that available in the water resource, which could be written as:

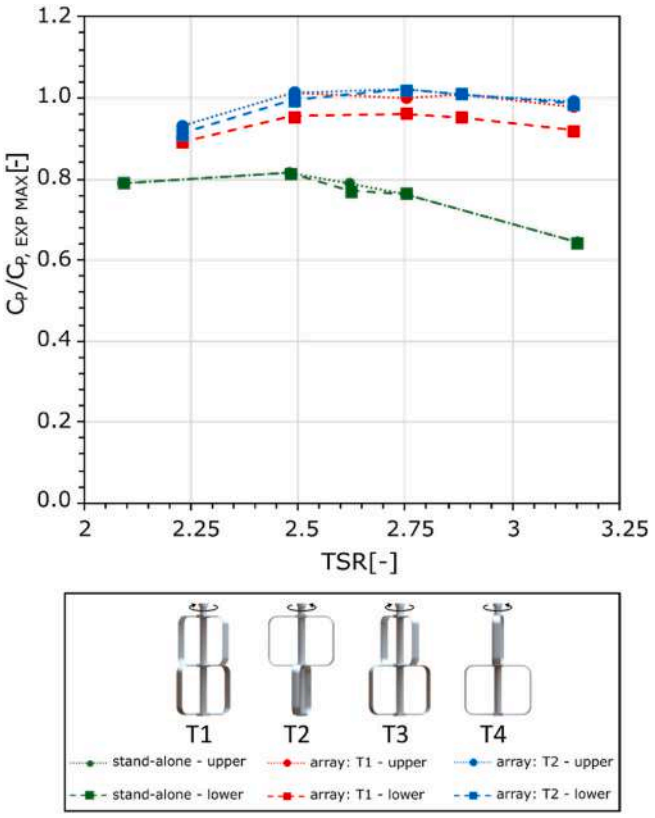

Fig. 16. Comparison between the average power coefficient normalized over the maximum experimental C_P for each rotor of the HKT design for the stand-alone turbine and the array.

$$C_P = \frac{P}{0.5\rho A V_\infty{}^3} \tag{3}$$

Where ρ is the water density, A is the turbine swept area, and V_∞ the freestream velocity. Concerning the latter, it can be noticed that the blockage affects the inflow velocity profiles as in Fig. 7-b, in which Cases II and III show slowdown in flow velocity compared to Case I, which is more pronounced at a distance 1D upstream. This decrease in the inflow velocity before the turbines should be considered while computing the power coefficient of the turbines C_P, otherwise the computed C_P would have an artificial increase that is not independent from Froude Number, as analyzed in detail in (Gauvin-Tremblay and Dumas, 2020). To this end, one can describe the flow at any channel cross-section plane in terms of its specific energy E:

$$E = \Delta h + \frac{V^2}{2g} \tag{4}$$

where Δh is the difference in the water surface altitude, V is the flow velocity, and g is the gravitational acceleration due to gravity, which was added to the model in the -Z direction. Thus, given the horizontal bed assumption, the initial boundary conditions at inlet could be written as $E_{inlet} = V_{inlet}{}^2/2g$, and a new parameter can be introduced to represent the effective flow velocity V_{eff} at any cross-section plan across the domain:

$$V_{eff} = \sqrt{2gE} \tag{5}$$

Fig. 8 reports the ratio between the effective flow velocity and the inlet velocity initially prescribed at inlet V_{eff}/V_{inlet} for both stand-alone turbine and an array of four turbines at different Tip-Speed Ratios (TSRs), the TSR is defined as the velocity of the turbine to the velocity of the inflow stream:

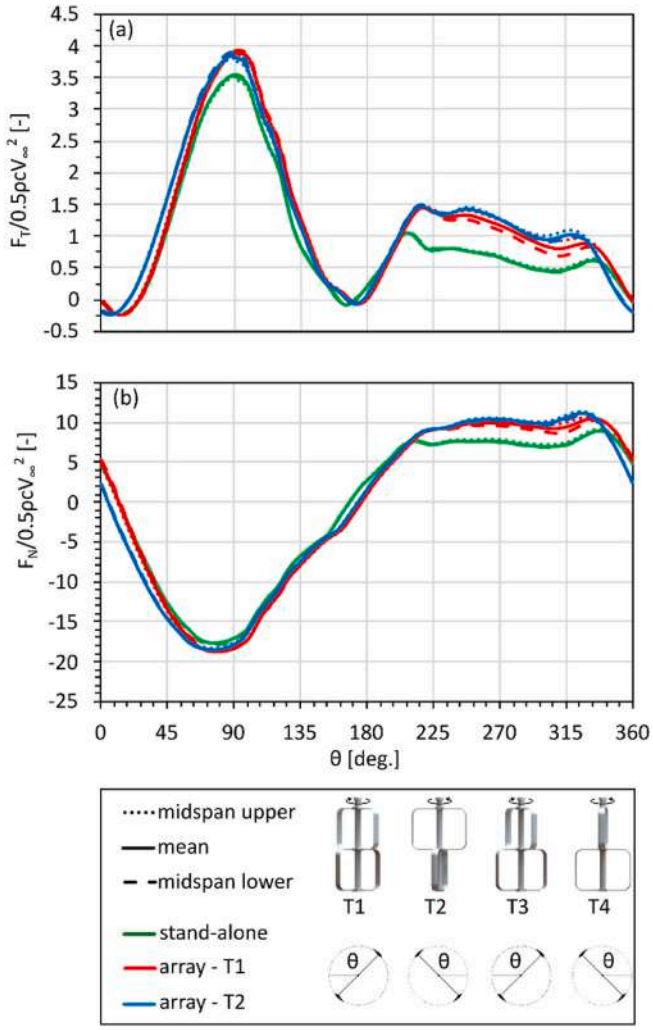

Fig. 17. Non dimensional (a) tangential and (b) normal forces on a single blade of the stand-alone turbine and the array.

$$TSR = \frac{\omega R}{V_\infty} \tag{6}$$

As can be seen, the specific energy upstream the turbines is higher than the one specified at inlet, then the energy decreases due to the power extracted from the turbine. It can be also noted that the total specific energy upstream is slightly above the one specified initially at inlet; this excess energy is indeed the effect of blockage, which should not be taken in consideration while computing the power coefficient. Thus, the velocity seen upstream the turbines, which is often less than the one defined at inlet, due to the presence of Δh, cannot be taken as a reference velocity to normalize the power coefficient as it does not represent the total specific energy available. Hence, V_{inlet} prescribed at inlet was considered to compute the C_P.

4.2. Domain size

In the domain sensitivity analysis, the goal was to investigate how varying the distances $L1$ and $L2$, as well as the height Z, affects both the performance of the turbines and the behaviour of the flow field. A total of eight different domains (detailed in Table 3), obtained by incrementally adjusting the values of $L1$, $L2$, and Z individually, were tested. All dimensions are normalized over the rotor diameter, D, for generality.

The coefficient of determination R^2 (see Eq. (7)) for the instantaneous torque, $C_T(\theta)$ was used to evaluate the independence of the

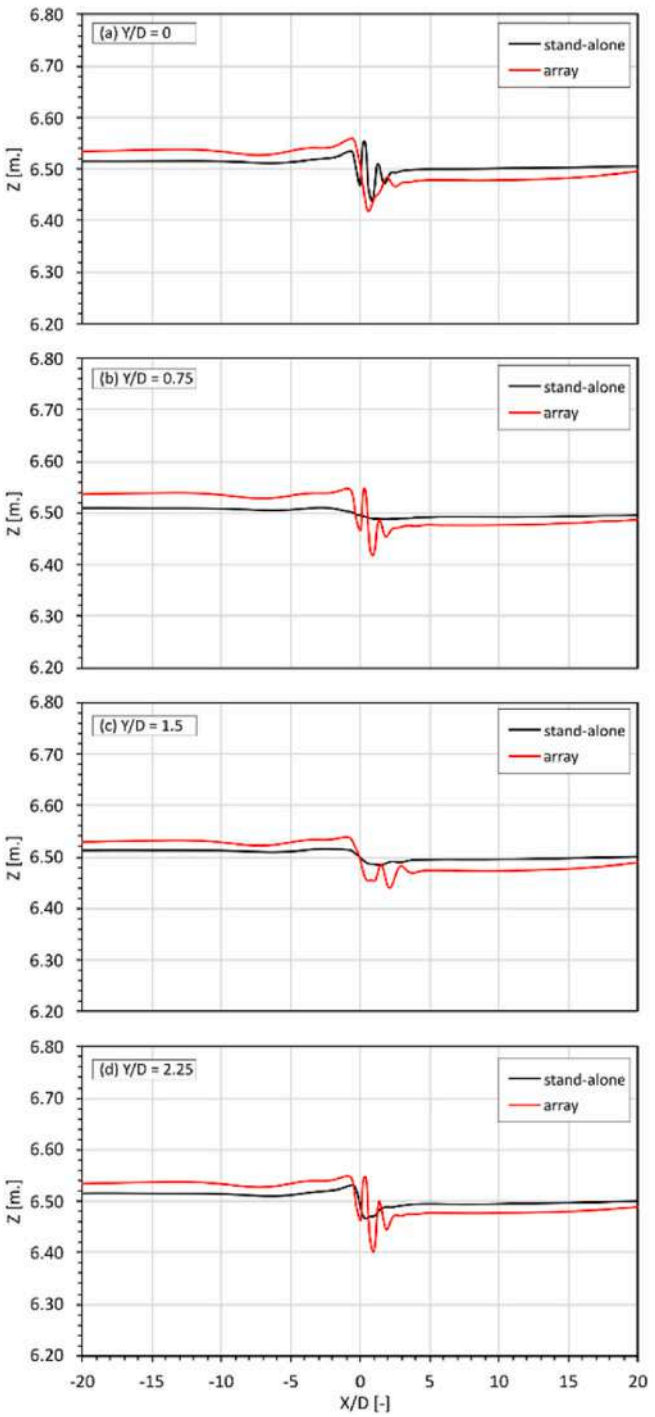

Fig. 18. Variation in water level at different lateral distances, comparison between stand-alone and array.

numerical solution with respect to a reference setup (subscript "final") (Balduzzi et al., 2016b), here identified with domains D1.2, D2.2, and D3.4 for the variables *Z*, *L1*, and *L2*, respectively.

$$R^2 = 1 - \frac{\sum_{\theta=0^\circ}^{360^\circ} \left[C_T(\theta) - C_{T,final}(\theta)\right]^2}{\sum_{\theta=0^\circ}^{360^\circ} \left[C_T(\theta) - C_{T,average}\right]^2} \quad (7)$$

Fig. 9 reports the R^2 results for the selected domains. Altering the height *Z* or the downstream distance *L2* has no significant impact on the resulting torque considering a threshold of $R^2 > 99.99\%$. However, variations in *L1* notably influence the turbine performance. It is important to note that, in the present simulation, and unlike the simulations that assume open field, the flow development upstream of the turbines, including the free surface rise, plays an important role in estimating the inflow conditions near upstream the turbines. Thus, sufficient upstream distance is required to guarantee the upstream flow fully development. Based on the results presented in this section, D3.3 was selected for the rest of the simulations.

4.3. Mesh independency test

A dedicated mesh sensitivity analysis was carried out to achieve a proper spatial discretization, aiming at the best compromise between accuracy in capturing spatial flow variations and computational efficiency. As shown in Fig. 10, the domain is discretized using a combination of hexahedral and tetrahedral mesh. The ALM region is discretized with structured mesh of uniform element size Δh. The streamwise distance as well as the height of the ALM region are divided into 30 divisions. Furthermore, 15 inflation layers were added near the channel walls to ensure that $y^+ < 1$. Table 4 displays the different grids that were evaluated. The analysis focused on three main parameters: (i) ALM element size Δh in terms of kernel width β, which was fixed at 0.25c for all cases; (ii) meshing strategy at the air-water interface, ensuring uniform hexahedral elements in this area; (iii) the number of divisions along *L1* and *L2*.

Fig. 11 illustrates the results of the mesh sensitivity analysis concerning water level, torque coefficient, and dimensionless velocity profiles. Initially, as depicted in Fig. 10-a), it is evident that, except for M1, the channel water level matches at the inlet and outlet for almost all other grids, with an upstream rise of approximately 0.04 m. Fig. 10-b) provides a more detailed profile of the water level within $-5 < X/D < 5$. Notably, almost no significant difference can be observed between case M2B and the other cases, suggesting the unnecessary use of structured mesh in the air-water interface for this case. The cyclic torque coefficient variation is shown in Fig. 10-c) for the evaluated meshes, indicating identical torque variation for all cases except M1, which exhibits some volatile variation around $\theta \approx 90^\circ$ and 225°. In Fig. 11, velocity profiles are depicted at the center of the channel for different distances upstream and downstream of the turbines. All grids exhibit similar velocity profiles upstream of the turbines. However, differences can only be noticed between M1 and the other grids, particularly at $X/D = 1$, highlighting the relative importance of properly sizing the ALM region. Nonetheless, the overall results are consistent for M2, M2B, and M3. Therefore, based on the above results, the mesh settings adopted for M2 were chosen for the rest of the simulations.

4.4. Convergence criteria

To ensure that the final solution is independent on the number of simulated revolutions, a dedicated analysis was carried out. As suggested in (Balduzzi et al., 2016a), two criteria were assessed: the first was based on the cyclic average power coefficient normalized by the final cycle's average power coefficient, while the second was based on the variation between the power coefficient of each cycle and that of the subsequent cycle. Based on literature recommendations and authors' experience, the convergence thresholds were set at 1.02 and ± 1%, respectively.

As shown in Fig. 12, the TSR plays a significant role during the initial phase of the simulation. At higher TSRs, initial cycles show greater divergence from the final solution. This divergence is linked to wake development. Conversely, for the same number of revolutions a lower TSR results in a longer simulated time, granting more time to the near wake to be convected downstream. Based on the analysis of Figs. 12 and 20 revolutions were found to be sufficient to reach the final solution, and this number was applied in all subsequent simulations.

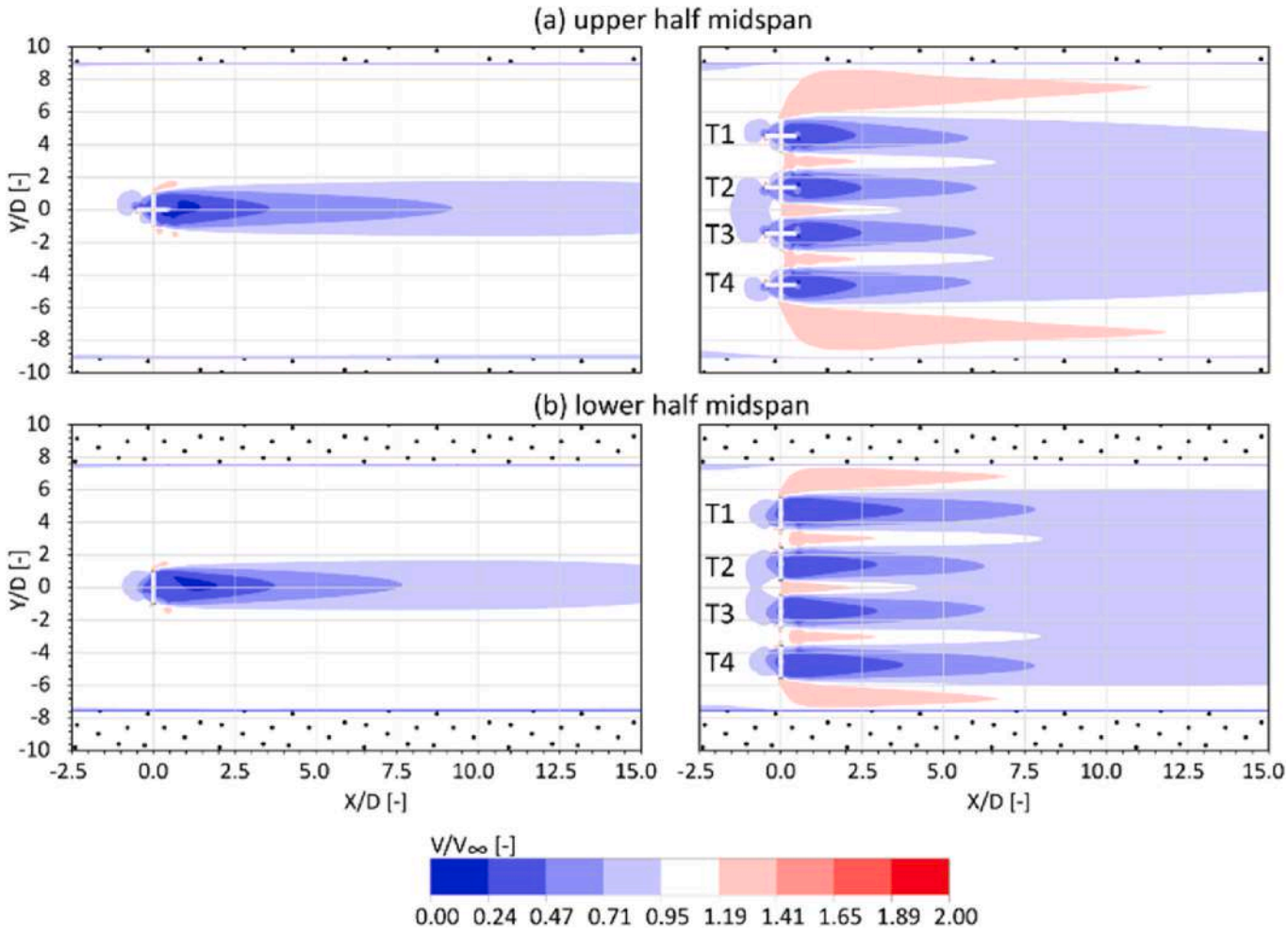

Fig. 19. a) dimensionless contours of the stand-alone turbine and the array at TSR = 2.75 plan view at mid-plane of lower and upper rotor.

5. Results and discussion

In this section, the main results obtained by the proposed numerical model are discussed. Initially, the validity of the model has been assessed by comparing its predictions against experimental measurements (see Section 5.1) Then, the performance of the HKT array is compared in Section 5.2 against the stand-alone turbine to assess the impact of deploying Darrieus turbines in close proximity in terms of efficiency improvement, as well as the influence on the channel itself and the flow field.

5.1. Validation

Fig. 13-a reports the experimental results of the average power coefficient, C_P of *T2* within the four-turbines array at various TSRs normalized over the maximum experimental C_P for *T2* (which occurs at TSR = 3.15), compared with that obtained from the present numerical model. Cp normalization is due to industrial non-disclosure constraints, although the normalization does not alter the comparative analyses presented in the study. In general, very good agreement is found between the numerical and experimental results at TSR ≥2.75, while at low TSRs, the numerical model shows overestimated power coefficient. Regarding the observed upstream rise reported in Fig. 13-b, it can be noticed that the experimental results show that ΔH is almost independent from the turbine rotational speed up to TSR ≈2.5. Thereafter, ΔH increases to its maximum value at TSR = 2.75, corresponds also to the maximum C_P, followed by a decrease and then an increase again. It can be noticed that the ΔH increase noticed at TSR >2.75 corresponds to an increase also in the C_P. This relation between the extracted power and the height of the upstream rise is not straightforward in the experimental results, as measurements at low TSRs does not show that. This might be attributed to uncertainties related to slight variations in the far upstream water level, which was not perfectly stationary during the measurement hours. However, the numerical model predictions showed a relation between the extracted power and ΔH, showing a degree of proportionality between the observed upstream rise hight and the computed C_P.

To validate the numerical model in terms of reproducing the water velocity flow field, Fig. 14-a depicts time-averaged vertical velocity profiles measured upstream of each turbine at X/D = −2.96 compared to the CFD results. It is evident that the inflow reproduced using ALM remains almost constant across the entire cross-sectional area, while experimental measurements exhibit some variations in velocity values. However, when comparing the velocity profiles, both CFD and experimental measurements demonstrate acceptable matching, indicating similarity in the inflow conditions. Some discrepancies are noticeable near the wall, which were attributed to the wall conditions used in the numerical simulation and the uncertainties in the experimental measurements near the wall.

In Fig. 14-b, velocity profiles sampled downstream of each turbine resulting from the ALM simulation are compared with those reconstructed using experimental measurements at a downstream distance of X/D = 6. Overall, a velocity deficit can be observed downstream of the turbines, with some acceleration regions appearing on the sides and at the channel bottom due to the blockage effect when the flow field

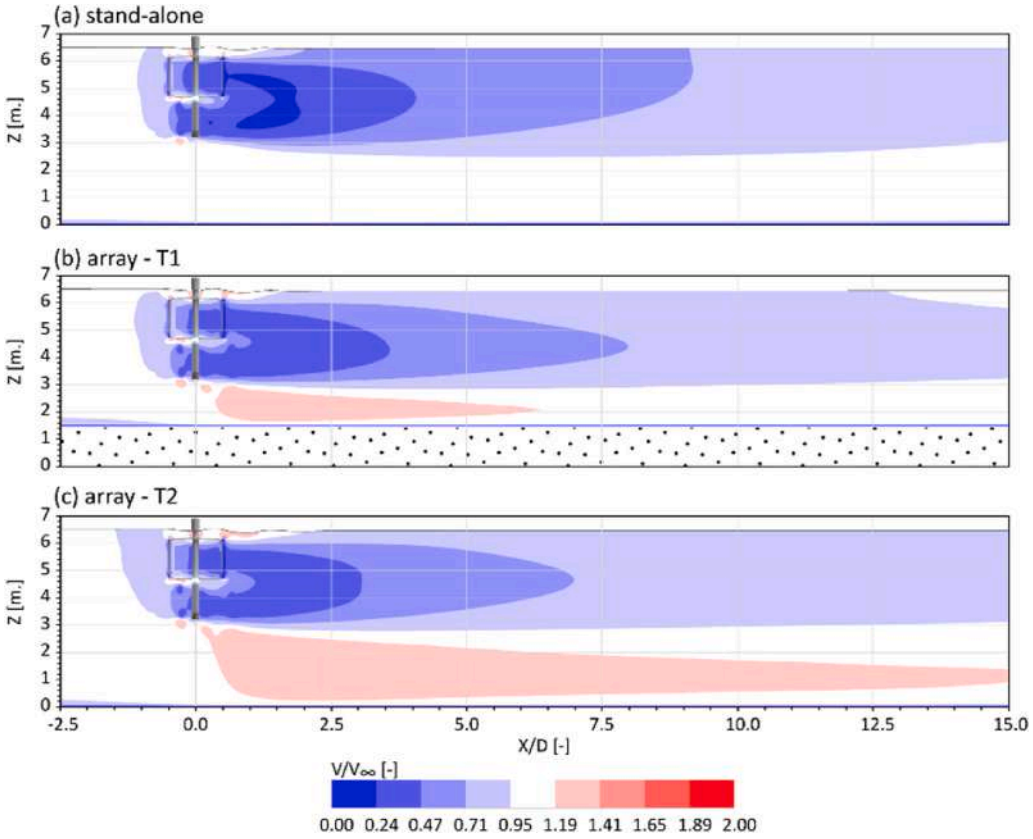

Fig. 20. Elevation view of the dimensionless velocity contours for the stand-alone compared with b) T1 and c) T2 in the array.

around the turbines interacts with the channel walls. The velocity profiles downstream of the turbines provide an indication of both the overall performance of the ALM and the effectiveness of its integration within a VOF solution. A general similarity is found in the shape of the velocity profiles. Discrepancies between the experimental and CFD results are noticeable near the walls, where uncertainties associated with the use of wall functions, in addition to experimental uncertainties in measurements near the wall, might be relevant.

Fig. 15 presents a comparison between the numerical model and the experimental measurements of velocity downstream from the center of T2 at various Z levels. Despite the significant variability observed in the experimental data, a discernible trend is evident. Overall, good agreement is achieved for X > 10 m. However, the near wake region is not accurately captured for the strut lines at Z = 6.2 m and 3.2 m, likely due to the unmodeled struts and the approximated tip-effect modeling, which ignores the curved blades at tips as detailed in section 3.2.1. Notably, there is a very strong agreement along the measurement line under the turbines (Z = 2.7 m), particularly in the acceleration region near the turbines.

5.2. HKT array performance

Moving to the analysis of the operational characteristics of the HKT design presented in this work along with the proposed array arrangement, Fig. 16 shows the average power coefficient for each turbine half in the array compared to the stand-alone turbine, normalized over the maximum experimental C_P for *T2*. Due to the symmetry in turbine performance, *T3* and *T4* produced identical results to *T2* and *T1*, respectively, so only the performance of *T1* and *T2* are presented.

In general, comparing the stand-alone turbine to the array shows that the efficiency of the array can be improved by up to 25%, with a shift in the optimum TSR from approximately 2.5 for the stand-alone turbine to 2.75 for the array. It is important to note that the performance curve of the array is almost flat between TSR values of 2.5 and 3.1. Additionally, for the turbines on the sides (*T1* and *T4*), the upper half produces more power than the lower half. In contrast, the turbines in the middle of the array (*T2* and *T3*) produce almost the same power in both halves, with only a small difference noticeable at low TSRs. This difference in C_P between the lower and upper halves of the side turbines is attributed to the trapezoidal shape of the channel, suggesting that the lower rotor experiences more flow interactions with the channel walls.

Fig. 17 shows the normalized instantaneous tangential F_T and normal F_N forces over one revolution for a single blade of *T1* and *T2* compared to that of the stand-alone turbine. For *T1*, where the mutual interaction is only with the adjacent *T2* in the inward half, the tangential force is similar to the stand-alone turbine during the first quarter ($0^\circ < \theta < 90^\circ$), with a higher peak at $\theta \approx 90^\circ$. During the second quarter ($90^\circ < \theta < 180^\circ$), *T1* shows a significant increase in tangential force compared to the stand-alone turbine due to the interaction with *T2*. An increase in the tangential force is also noted during the downstream half ($180^\circ < \theta < 360^\circ$). The differences in tangential force between the upper and lower halves are more pronounced during the downstream half of the revolution.

Similar observations are made for the normal force on *T1*. The normal force closely matches that of the stand-alone turbine during the first quarter, with no mutual interaction with other turbines. However, during the second quarter, the normal force of *T1* is significantly higher than that of the stand-alone turbine, and the differences between the upper and lower halves are more pronounced during the downwind half of the revolution.

On the other hand, *T2* exhibited higher tangential and normal forces on both the windward and leeward sides compared to the stand-alone turbine, due to its mutual interaction with *T1* and *T3*. Throughout the entire downwind half, the forces on the turbine blade were of greater magnitude, slightly exceeding those of *T1* at most downstream azimuth positions.

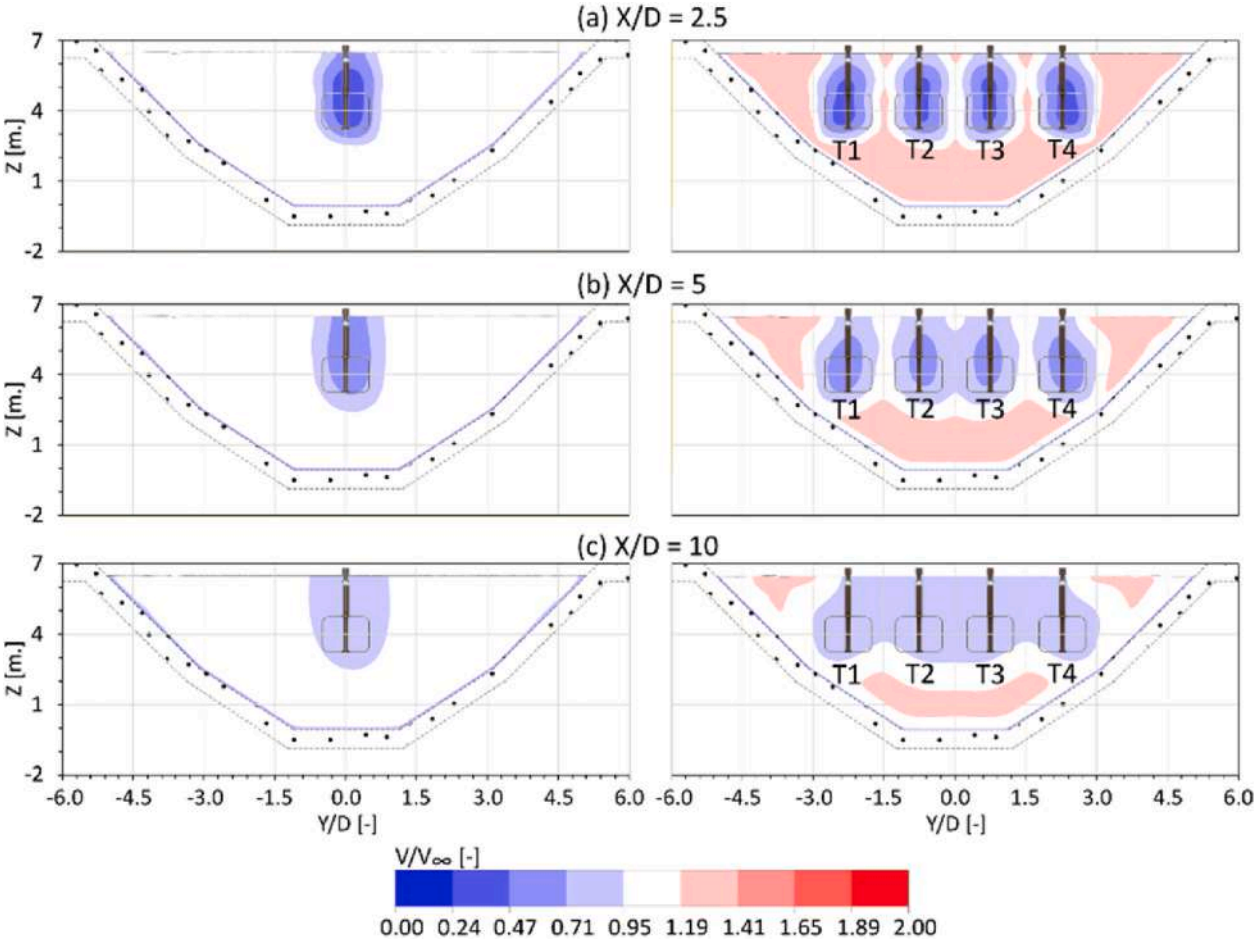

Fig. 21. Front view of the dimensionless velocity contours for the a) stand-alone turbine, b) T1 and c) T2 in the array.

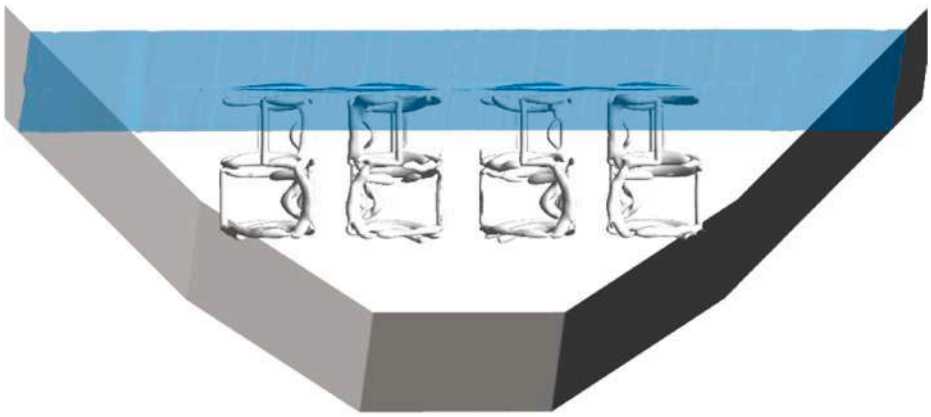

Fig. 22. Two iso surfaces for λ_2 criterion showing the vortex cores resulting from the four-turbine array, and the free water surface.

5.3. Hydraulic impact on the channel

To investigate the impact of deploying HKTs on the channel itself, instantaneous water level variations after the 20th cycle are reported for both the stand-alone turbine and the array case at various Y/D distances, as shown in Fig. 18. Since the solution is symmetrical around the channel vertical longitudinal mid-plane, only positive Y/D values are reported, with the corresponding negative values being equal. As seen, deploying the array results in a significantly higher upwind rise across all Y/D sections. In contrast, the blockage induced by the stand-alone turbine is not sufficient to significantly raise the water level, especially on the sides, far from the turbine located at the channel centre. For the stand-alone turbine, the average upstream rise along the canal width is approximately 0.06 m, peaking at about 0.12 m at the centre. On the other hand, the average upstream rise for the array is 0.13 m, with minimal deviation from the peak value at the channel centre, which is 0.14 m.

Fig. 19 shows the velocity contour, made non-dimensional by the inlet velocity V_∞, in the top view for the mid-plane of both the lower and upper turbine of the stand-alone turbine and the four-turbine array. The blockage effect is evident in the array case, with accelerated flow observed between the turbines themselves as well as between the

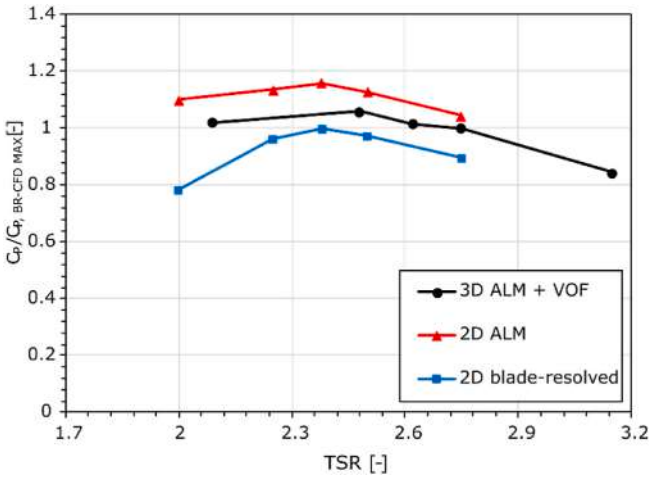

Fig. 23. Comparison between the average power coefficient C_P normalized over maximum C_P of the blade-resolved CFD for the stand-alone turbine using 2D ALM, 3D ALM and blade-resolved CFD.

turbines and the channel wall on the sides. The difference in accelerated flow between the upper and lower halves of the array is significant; the upper half experiences more intense acceleration zones compared to the lower half. It is important to note that the lower parts of the turbines are subjected to a smaller cross-sectional channel area due to the trapezoidal shape. However, this difference is not sufficient to cause a significant impact on the wake dissipation mechanism or the power coefficient.

Fig. 20 shows the elevation view of the dimensionless velocity contour for the stand-alone turbine compared with T1 and T2 within the array. Slightly faster wake dissipation can be observed in the array case compared to the stand-alone turbine, particularly near the free water surface at X/D > 2.5. More importantly, an acceleration zone forms below the turbines in the array, with velocities reaching about $1.2V_\infty$. This acceleration zone is due to flow blockage, where the inflow anticipated by the turbines is bypassed below the array, causing significant acceleration, which is not present in the stand-alone turbine case.

Fig. 21 shows the dimensionless velocity contours from the front view at several channel cross-sections for X/D = 2.5, 5, and 10. It can be seen that this acceleration zone remains around the turbines up to X/D = 10, after which the wake gradually returns to V_∞. Another observation from these contours is the shape of the wake produced by this design, which has two connected parts. This enhances the mixing of the wake and does not exhibit the typical skewed wake shape known for VATs (see Fig. 22).

From the analysis, it is evident that deploying an array of HKTs increases the local acceleration zones in the channel near the turbines, significantly higher than the stand-alone turbine due to the imposed blockage, particularly between the turbines and the channel bed in the

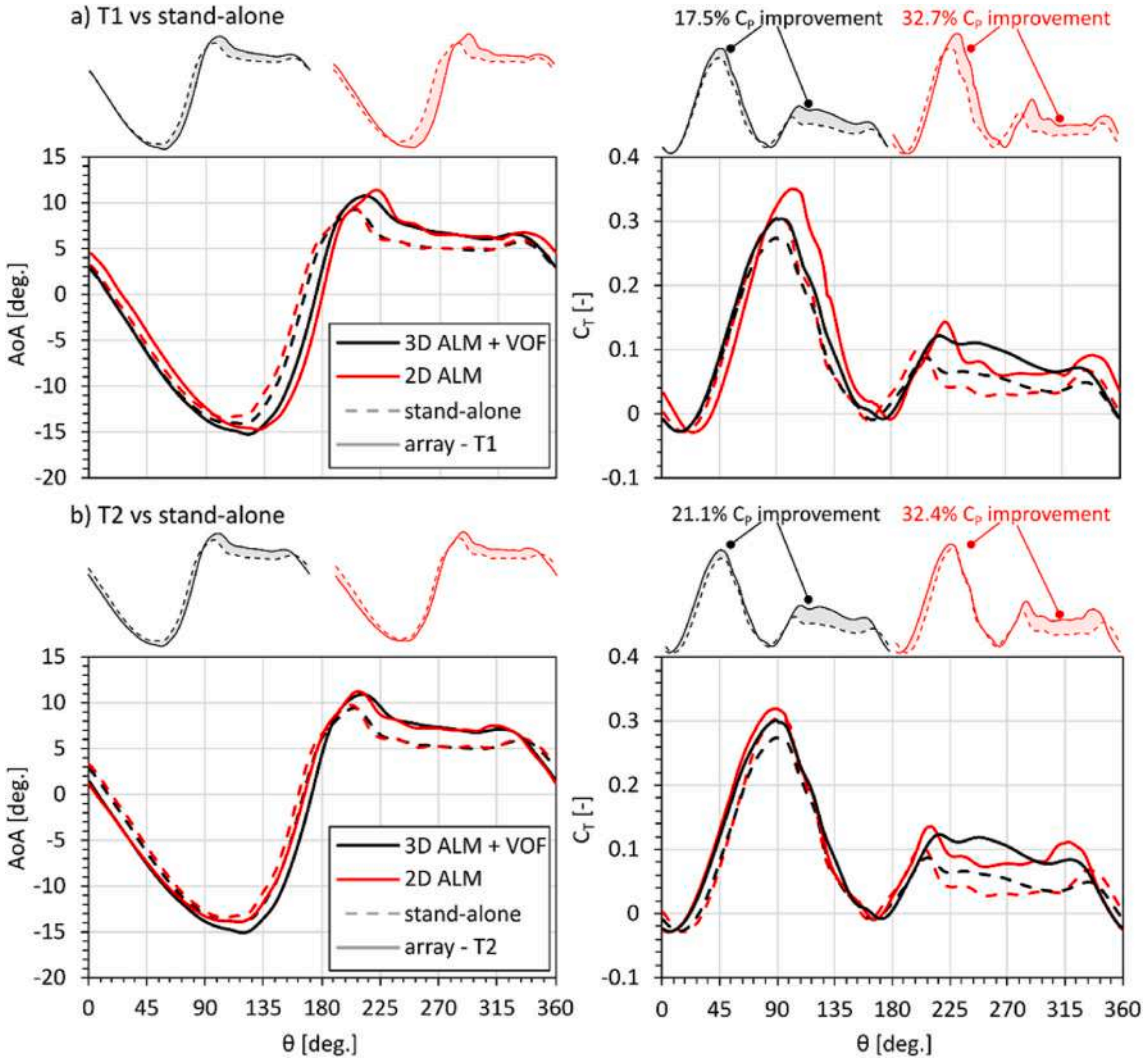

Fig. 24. Comparison between the 3D and the 2D ALM in terms of the capability of capturing the power augmentation in an array: stand-alone vs a) T1 and b) T2.

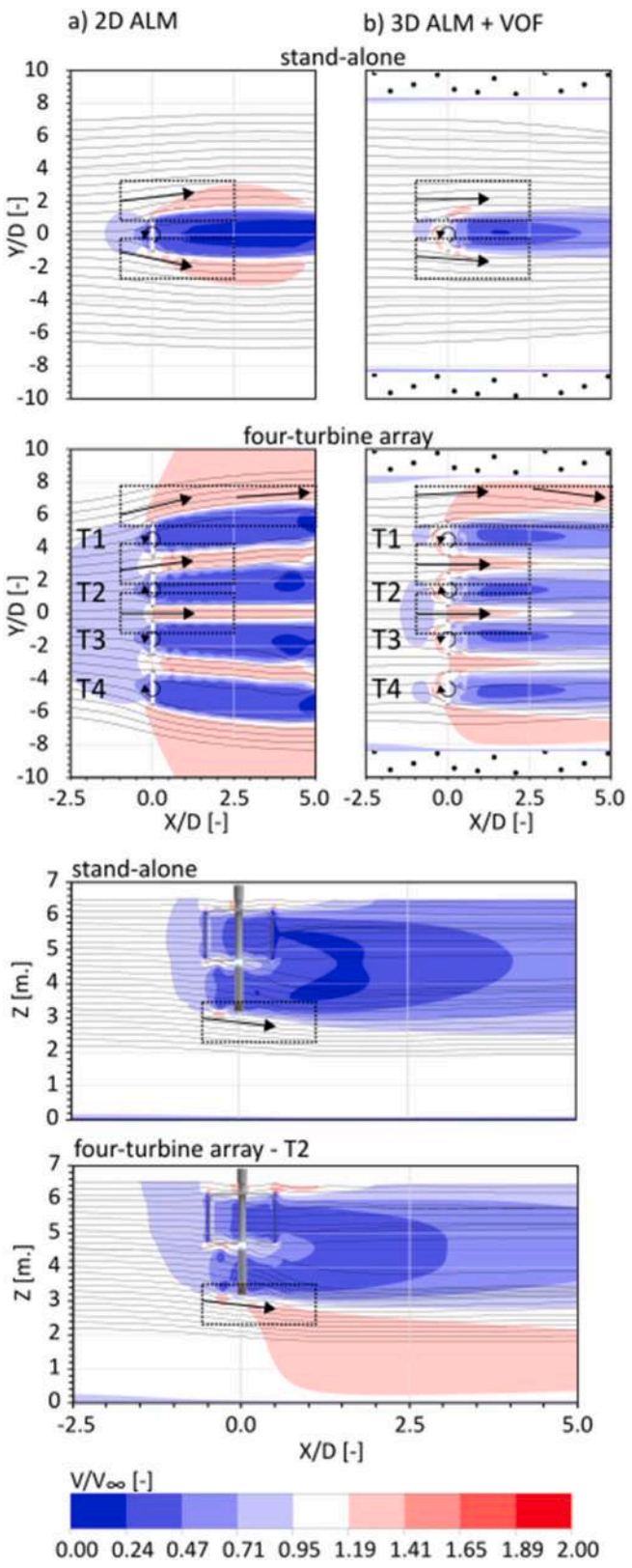

Fig. 25. Contours of dimensionless velocity and streamlines for the 2D ALM and the 3D ALM for stand-alone turbine and array.

wake area. In the case in hand, the acceleration zone did not present a significant risk to the channel, with $V_{max} \approx 1.2V_{\infty}$. However, this aspect must be carefully considered when designing an array of HKTs and tested for its impact, especially at high TSR operation of the turbines, due to the potential long-term risks, such as erosion of the channel walls.

5.4. Power enhancement in arrays: 2D vs 3D

Fig. 23 presents the average cyclic C_P at different TSRs for the stand-alone turbine using three different simulation techniques: a) 2D blade-resolved CFD (Mohamed et al., 2023a), which is the conventional and widely used method for simulating Darrieus turbines; b) 2D ALM, using the latest formulation employed in the present and previous studies (Melani et al., 2021a; Mohamed et al., 2022, 2023b); and c) the present 3D ALM coupled with VOF.

Upon comparison of the results, one can notice that adding the three-dimensional effects as well as the influence of the free water surface makes the solution of the ALM close to that of the blade-resolved CFD. However, it can also be seen that at low TSRs, both the 2D and 3D ALM show a higher C_P, which is attributed to the known incapability of the Berg dynamic stall model to accurately reproduce the lift hysteresis, especially during the downwind half, resulting in overestimated power. This issue was previously discussed in detail by some of the authors in (Mohamed et al., 2022). The lower the TSR, the more this issue persists due to the relevance of the unsteady effects associated with the wide range of AoA seen by the turbine blades. At high TSRs, on the other hand, the presence of dynamic effects under attached flow conditions is also relevant. These effects are not considered in the Berg model, resulting in a slight overprediction of the power coefficient compared to blade-resolved CFD. (Melani et al., 2021a), (Mohamed et al., 2022)., (Mohamed et al., 2023b)

As reported by some of the authors (Mohamed et al., 2023a) in a recent two-dimensional analysis using a blade-resolved CFD, deploying closely spaced Darrieus rotors in an inline layout creates a blockage that straightens the inflow and eliminates the streamtube expansion effect between adjacent rotors. This leads to an increase in the AoA and consequently, the lift force and produced torque, while also shifting the optimum power coefficient towards higher TSRs. Given that the present ALM code has demonstrated a strong capability in replicating this mechanism (Mohamed et al., 2023b), the power augmentation resulting from clustering the turbines can be more accurately assessed using the present CFD model.

To investigate this in detail, Fig. 24 illustrates the percentage improvement for each of the codes and compares their results for the instantaneous variations of the torque coefficient and angle of attack for a single blade of *T1* and *T2* in the four-turbine array against the stand-alone turbine. For *T1*, the power coefficient improvement is nearly doubled in the 2D and open (assumed infinite) domain due to the increased AoA within the mutual interaction area ($90^\circ > \theta > 270^\circ$). This increase in AoA, evidently is overestimated in the 2D case, especially in the second upwind quarter ($90^\circ > \theta > 180^\circ$). For *T2*, the differences between the 2D and 3D code estimations are less pronounced. It is important to note that for both *T1* and *T2*, the performance improvement in the downwind half might be exaggerated, as detailed in (Mohamed et al., 2023b), which compared the present ALM code with blade-resolved CFD. It suggests that the discrepancy in blade loads during the downstream half is due to the ALM algorithm, particularly the Berg dynamic stall model, at which a good matching between the lift hysteresis was found between both ALM and blade-resolved simulations during pitch-up. However, in the downwind part, the ALM maintains a linear behaviour, whereas the computed blade-resolved data showed a reduction in the nominal slope and a lag in the instantaneous lift relative to the AoA.

Fig. 25 shows the dimensionless velocity contours and streamlines around both the stand-alone turbine and the four-turbine array, using 2D and 3D ALM. In the stand-alone turbine case, the 3D simulation does not exhibit the same degree of flow deviation in front of the turbine as the 2D simulation, where turbine blades are assumed to be infinite in the Z-direction. In the 2D case, this deviation is more apparent, showing more accelerated flow near the shear layers in the wake. Conversely, in

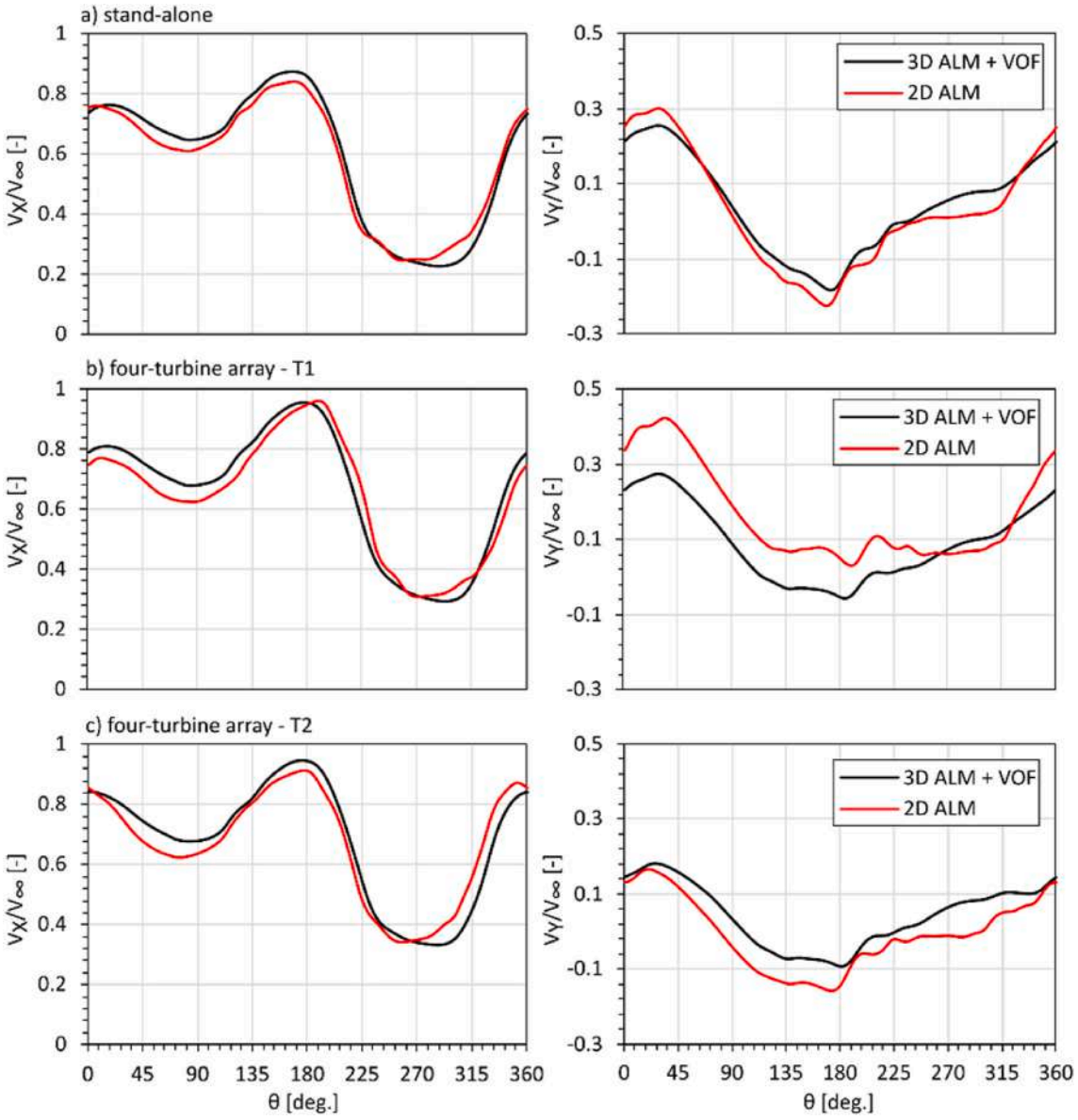

Fig. 26. Comparison between the Vx and Vy local to the blade in stand-alone and array 2D vs 3D ALM.

the 3D case, the elevation view in Fig. 19-b.2) reveals how the streamtube expansion is distributed among the three dimensions, with the flow deviating toward the ground. This reduces the impact of streamtube expansion in the plane view. This observation suggests that 2D simulations may be less valid for hydrokinetic turbines, given their relatively small aspect ratio compared to their wind counterparts. Additionally, the design of the channel itself plays an important role in this behaviour.

Moving to the four-turbine array, the behaviour of inflow deviation in front of the turbines on the sides differs significantly between the 3D and 2D cases. In the 3D scenario, the flow stream is confined by the channel walls, compelling it to straighten.

Conversely, in the 2D scenario, notable inflow deviation is observed on sides of the array, which accounts for the differences in sampled angle of attack variation for *T1* between the 2D and 3D results. Additionally, at X/D = 2.5, the wake in the 3D case converges toward the wake core, while in the 2D case, it diverges. For *T2*, the differences in inflow deviation are less pronounced, with only a slightly more deviated inflow in the interaction area between *T1* and *T2*, corresponding to the smaller differences in the estimated power coefficient of *T2* between the 3D and 2D simulations. Notably, the degree of inflow vertical deviation for *T2* resembles that of the stand-alone turbine, despite the presence of a large acceleration zone extending up to the channel ground walls, imposed by the array blockage.

To elaborate on the previous observations, the local inflow velocity components are compared for the 2D and 3D ALM, these data were obtained using the LineAverage method explained in section 3.2.1. Fig. 26 shows the variation in the nondimensionalized X and Y velocities sampled in front of a single blade of *T1* and *T2* compared to the stand-alone turbine, obtained using both 2D and 3D ALM. For the stand-alone turbine, V_x is slightly higher in the 3D case, with lower V_y due to less flow deviation. For *T1* in the array, a slight phase shift can be observed in the V_x of the 3D case, along with significant differences in V_y during the upwind half. This indicates less inflow deviation due to the blockage imposed by the channel walls in the first quarter ($0^\circ > \theta > 90^\circ$) and interaction with *T2* in the second quarter ($90^\circ > \theta > 180^\circ$), explaining the significant differences in C_P and the shift in instantaneous C_T between the 2D and 3D results. The phase shift in the mutual interaction region between *T1* and *T2* is not captured by the 2D simulation because *T1* is heavily affected by blockage dur to channel walls. However, the V_x between *T2* and *T3* shows a similar trend in both 3D and 2D

simulations ($0^\circ > \theta > 90^\circ$ and $270^\circ > \theta > 360^\circ$ in the *T2* results), suggesting minimal wall blockage effects. The primary blockage is caused by the turbine clustering, which is well captured in the 2D simulation.

6. Conclusions

This study introduces a medium-fidelity model for analysing the performance of an array of Darrieus-type HKTs in an open channel, employing the ALM coupled with the VOF method via U-RANS solver. A sensitivity analysis addressed the main modelling features for open channels and the necessary corrections for efficiency calculations considering water surface variations. Numerical sensitivity assessments were performed, followed by a validation campaign against experimental measurements for turbine performance, water level, and flow field velocities. Then, the study delved into turbine performance and the power augmentation mechanism from clustering turbines in close proximity. Furthermore, the hydraulic impact of the turbine array on the channel was examined, addressing potential concerns when installing turbine arrays in channels.

Overall, among the various simulation techniques for the Darrieus turbine, the proposed CFD model offers the best trade-off between accuracy and computational time. The following points summarize the main findings of the study:

- Coupling the ALM with the VOF can improve predictions of turbine performance, particularly at high TSRs, by accounting for the variations in the free water surface. However, at low TSRs, the accuracy of the ALM decreases due to unsteady effects that are not fully captured by the Berg dynamic stall model used for the present analysis.
- Good agreement was found between the experimental velocity measurements and the ALM results, especially in the near wake area. However, discrepancies in the longitudinal wake measurements at the turbine tip were observed, possibly due to lack of struts modelling. This issue will be addressed in future work.
- When simulating HKTs assuming a horizontal-bed open channel, the initial inlet velocity should be used to compute turbine power coefficients, as velocities in front of turbines are affected by blockage, e.g., $\approx 0.9V_{inlet}$ for single turbine and $\approx 0.86V_{inlet}$ for the four-turbine cluster, thus overestimating efficiency.
- When doing a CFD simulation for HKTs in open channels, greater distance between turbines and inlet is necessary for flow to fully develop, while distance between turbines and outlet is less critical.
- The HKT array in this study resulted in up to 25% more power than stand-alone turbines due to combined blockage effects from channel walls and neighbouring turbines. Additionally, the optimum TSR shifted toward a higher value.
- Realistic simulations considering channel boundaries and free water surface show significant differences between 2D and 3D turbine models, with 2D simulations exaggerating power augmentation effects, e.g., 32% maximum power augmentation in 2D compared to a corresponding 21% for the 3D.
- Although installing Darrieus-type HKTs in close proximity enhances efficiency, turbine arrays create acceleration zones near channel walls more than stand-alone turbines, requiring careful consideration for long-term impacts on the channel. The use of 3D models like the one proposed here is strongly recommended in these applications.

Future work should focus on enhancing the accuracy of ALM predictions, particularly at low TSRs, by incorporating more advanced dynamic stall models. Additionally, a more thorough investigation of tip effects in simulations is needed to improve overall model fidelity.

CRediT authorship contribution statement

Omar S. Mohamed: Writing – original draft, Visualization, Validation, Software, Methodology, Investigation, Formal analysis, Data curation. **Pier Francesco Melani:** Writing – review & editing, Visualization, Software, Methodology. **Giuseppe Soraperra:** Writing – review & editing, Resources, Investigation. **Alessandra Brighenti:** Writing – review & editing, Resources, Investigation. **Giovanni Ferrara:** Writing – review & editing, Supervision, Project administration. **Vittorino Betti:** Project administration, Funding acquisition. **Leonardo Schippa:** Writing – review & editing, Investigation. **Massimo Guerrero:** Writing – review & editing, Investigation. **Francesco Balduzzi:** Writing – review & editing, Methodology, Conceptualization. **Alessandro Bianchini:** Writing – review & editing, Resources, Project administration, Methodology, Investigation, Funding acquisition, Data curation, Conceptualization.

Declaration of competing interest

The authors declare that they have no known competing financial interests or personal relationships that could have appeared to influence the work reported in this paper.

Acknowledgments

Thanks are due to HE-Powergreen for the support in the PhD of Omar Sherif Mohamed and for sharing experimental measurements.

References

Bachant, P., Goude, A., Wosnik, M., 2018. Actuator Line Modeling of Vertical-axis Turbines. https://doi.org/10.48550/arXiv.1605.01449 arXiv, arXiv:1605.01449.

Balduzzi, F., Bianchini, A., Maleci, R., Ferrara, G., Ferrari, L., 2016a. Critical issues in the CFD simulation of Darrieus wind turbines. Renew. Energy 85, 419–435. https://doi.org/10.1016/j.renene.2015.06.048.

Balduzzi, F., Bianchini, A., Ferrara, G., Ferrari, L., 2016b. Dimensionless numbers for the assessment of mesh and timestep requirements in CFD simulations of Darrieus wind turbines. Energy 97, 246–261. https://doi.org/10.1016/j.energy.2015.12.111.

Balduzzi, F., Melani, P.F., Soraperra, G., Brighenti, A., Battisti, L., Bianchini, A., 2021. Some design guidelines to adapt a Darrieus vertical axis turbine for use in hydrokinetic applications. E3S Web Conf. 312, 08017. https://doi.org/10.1051/e3sconf/202131208017.

Cacciali, L., Battisti, L., Dell'Anna, S., 2022. Free surface double actuator disc theory and double Multiple streamtube model for in-stream Darrieus hydrokinetic turbines. Ocean Eng. 260, 112017. https://doi.org/10.1016/j.oceaneng.2022.112017.

Cacciali, L., Battisti, L., Dell'Anna, S., 2023a. Backwater assessment for the energy conversion through hydrokinetic turbines in subcritical prismatic canals. Ocean Eng. 267, 113246. https://doi.org/10.1016/j.oceaneng.2022.113246.

Cacciali, L., Battisti, L., Dell'Anna, S., 2023b. Multi-array design for hydrokinetic turbines in hydropower canals. Energies 16 (5), 5. https://doi.org/10.3390/en16052279.

Chaulagain, R.K., Poudel, L., Maharjan, S., 2023. A review on non-conventional hydropower turbines and their selection for ultra-low-head applications. Heliyon 9 (7), e17753. https://doi.org/10.1016/j.heliyon.2023.e17753.

Chen, Y., Guo, P., Zhang, D., Chai, K., Zhao, C., Li, J., 2022. Power improvement of a cluster of three Savonius wind turbines using the variable-speed control method. Renew. Energy 193, 832–842. https://doi.org/10.1016/j.renene.2022.05.062.

de Boor, C., 1978. A practical guide to splines. In: Applied Mathematical Sciences. Springer-Verlag, New York [Online]. Available: https://www.springer.com/gp/book/9780387953663. (Accessed 23 November 2020).

Draper, S., Nishino, T., 2014. Centred and staggered arrangements of tidal turbines. J. Fluid Mech. 739, 72–93. https://doi.org/10.1017/jfm.2013.593.

Gauvin-Tremblay, O., Dumas, G., 2020. Two-way interaction between river and deployed cross-flow hydrokinetic turbines. J. Renew. Sustain. Energy 12 (3), 034501. https://doi.org/10.1063/5.0004492.

Guerrero, M., Conevski, S., Cavalieri, I., Schippa, L., Ruther, N., 2023. Influence of hydropower propellers on open-channel flow. J. Hydraul. Eng. 149 (11), 04023047. https://doi.org/10.1061/JHEND8.HYENG-13417.

Hirt, C.W., Nichols, B.D., 1981. Volume of fluid (VOF) method for the dynamics of free boundaries. J. Comput. Phys. 39 (1), 201–225. https://doi.org/10.1016/0021-9991(81)90145-5.

Jost, E., Klein, L., Leipprand, H., Lutz, T., Krämer, E., 2018. Extracting the angle of attack on rotor blades from CFD simulations. Wind Energy 21 (10), 807–822. https://doi.org/10.1002/we.2196.

Kirke, B., 2019. Hydrokinetic and ultra-low head turbines in rivers: a reality check. Energy Sustai. Deve. 52, 1–10. https://doi.org/10.1016/j.esd.2019.06.002.

Marten, D., et al., 2016. Effects of airfoil's polar data in the stall region on the estimation of Darrieus wind turbines performance. J. Eng. Gas Turbines Power 139 (2), 22606–22609. https://doi.org/10.1115/1.4034326.

Massé, B., 1981. Description de deux programmes d'ordinateur pour le calcul des performances et des charges aérodynamiques pour les éoliennes à axe vertical technical report IREQ-2379.

Melani, P.F., 2018. Experimental assessment of an actuator line simulation tool for vertical axis wind turbines [Online]. Available: https://www.politesi.polimi.it/handle/10589/141629. (Accessed 5 September 2024).

Melani, P.F., Balduzzi, F., Ferrara, G., Bianchini, A., 2020. How to extract the angle attack on airfoils in cycloidal motion from a flow field solved with computational fluid dynamics? Development and verification of a robust computational procedure. Energy Convers. Manag. 223, 113284. https://doi.org/10.1016/j.enconman.2020.113284.

Melani, P.F., Balduzzi, F., Ferrara, G., Bianchini, A., 2021a. Tailoring the actuator line theory to the simulation of Vertical-Axis Wind Turbines. Energy Convers. Manag. 243, 114422. https://doi.org/10.1016/j.enconman.2021.114422.

Melani, P.F., Balduzzi, F., Ferrara, G., Bianchini, A., 2021b. Development of a desmodromic variable pitch system for hydrokinetic turbines. Energy Convers. Manag. 250, 114890. https://doi.org/10.1016/j.enconman.2021.114890.

Melani, P.F., Balduzzi, F., Bianchini, A., 2021c. A robust procedure to implement dynamic stall models into actuator line methods for the simulation of vertical-Axis wind turbines. J. Eng. Gas Turbines Power 143 (11). https://doi.org/10.1115/1.4051909.

Melani, P.F., Balduzzi, F., Bianchini, A., 2022. Simulating tip effects in vertical-axis wind turbines with the actuator line method. J. Phys.: Conf. Ser. 2265 (3), 032028. https://doi.org/10.1088/1742-6596/2265/3/032028.

Melani, P.F., Mohamed, O.S., Cioni, S., Balduzzi, F., Bianchini, A., 2024a. An insight into the capability of the actuator line method to resolve tip vortices. Wind Energy Sci. 9 (3), 601–622. https://doi.org/10.5194/wes-9-601-2024.

Melani, P.F., Mohamed, O.S., Cioni, S., Balduzzi, F., Bianchini, A., 2024b. Tuning the actuator line method to properly modelling tip effects in finite-length blades. J. Phys.: Conf. Ser. 2767 (5), 052018. https://doi.org/10.1088/1742-6596/2767/5/052018.

Menter, F.R., 1993. Zonal two equation kappa-omega turbulence models for aerodynamic flows. Presented at the AIAA Fluid Dynamics Conference. Orlando, FL. https://ntrs.nasa.gov/citations/19960044572. (Accessed 19 April 2023).

Menter, F.R., Smirnov, P.E., Liu, T., Avancha, R., 2015. A one-equation local correlation-based transition model. Flow, Turbul. Combust. 95 (4), 583–619. https://doi.org/10.1007/s10494-015-9622-4.

Mohamed, O.S., Ibrahim, A., El Baz, A.M.R., 2019. CFD investigation of the Multiple rotors Darrieus type turbine performance. Presented at the ASME Turbo Expo 2019: Turbomachinery Technical Conference and Exposition. American Society of Mechanical Engineers Digital Collection. https://doi.org/10.1115/GT2019-91491.

Mohamed, O.S., Elbaz, A.M.R., Bianchini, A., 2021. A better insight on physics involved in the self-starting of a straight-blade Darrieus wind turbine by means of two-dimensional Computational Fluid Dynamics. J. Wind Eng. Ind. Aerod. 218, 104793. https://doi.org/10.1016/j.jweia.2021.104793.

Mohamed, O.S., Melani, P.F., Balduzzi, F., Ferrara, G., Bianchini, A., 2022. An insight on the key factors influencing the accuracy of the actuator line method for use in vertical-axis turbines: limitations and open challenges. Energy Convers. Manag. 270, 116249. https://doi.org/10.1016/j.enconman.2022.116249.

Mohamed, O.S., Melani, P.F., Balduzzi, F., Ferrara, G., Bianchini, A., 2023a. An insight on the physical mechanisms responsible of power augmentation in a pair of counter-rotating Darrieus turbines. Energy Convers. Manag. 284, 116991. https://doi.org/10.1016/j.enconman.2023.116991.

Mohamed, O.S., Melani, P.F., Papi, F., Balduzzi, F., Bianchini, A., 2023b. Is the Actuator line method able to reproduce the interaction between closely-spaced Darrieus rotors? a critical assessment on wind and hydrokinetic turbines. Energy Convers. Manag. 293. https://doi.org/10.1016/j.enconman.2023.117473.

Myers, L., Bahaj, A.S., 2007. Wake studies of a 1/30th scale horizontal axis marine current turbine. Ocean Eng. 34 (5), 758–762. https://doi.org/10.1016/j.oceaneng.2006.04.013.

Nag, A.K., Sarkar, S., 2021. Performance analysis of Helical Savonius Hydrokinetic turbines arranged in array. Ocean Eng. 241, 110020. https://doi.org/10.1016/j.oceaneng.2021.110020.

Niebuhr, C.M., van Dijk, M., Neary, V.S., Bhagwan, J.N., 2019. A review of hydrokinetic turbines and enhancement techniques for canal installations: technology, applicability and potential. Renew. Sustain. Energy Rev. 113, 109240. https://doi.org/10.1016/j.rser.2019.06.047. Oct.

Nishi, Y., Sato, G., Shiohara, D., Inagaki, T., Kikuchi, N., 2017. Performance characteristics of axial flow hydraulic turbine with a collection device in free surface flow field. Renew. Energy 112, 53–62. https://doi.org/10.1016/j.renene.2017.04.047.

Nishino, T., Willden, R.H.J., 2012. The efficiency of an array of tidal turbines partially blocking a wide channel. J. Fluid Mech. 708, 596–606. https://doi.org/10.1017/jfm.2012.349.

Nishino, T., Willden, R.H.J., 2013. Two-scale dynamics of flow past a partial cross-stream array of tidal turbines. J. Fluid Mech. 730, 220–244. https://doi.org/10.1017/jfm.2013.340.

Rainbird, J.M., et al., 2015. On the influence of virtual camber effect on airfoil polars for use in simulations of Darrieus wind turbines. Energy Convers. Manag. 106, 373–384. https://doi.org/10.1016/j.enconman.2015.09.053.

Sørensen, J.N., Shen, W.Z., 2002. Numerical modeling of wind turbine wakes. J. Fluid Eng. 124 (2), 393–399. https://doi.org/10.1115/1.1471361.

Sørensen, J.N., Dag, K.O., Ramos-García, N., 2014. A new tip correction based on the decambering approach. J. Phys.: Conf. Ser. 524 (1), 012097. https://doi.org/10.1088/1742-6596/524/1/012097.

Viterna, L.A., Janetzke, D.C., 1982. Theoretical and Experimental Power from Large Horizontal-Axis Wind Turbines. NASA Technical Memorandum.

Yadav, P.K., Kumar, A., Jaiswal, S., 2023. A critical review of technologies for harnessing the power from flowing water using a hydrokinetic turbine to fulfill the energy need. Energy Rep. 9, 2102–2117. https://doi.org/10.1016/j.egyr.2023.01.033.

Yosry, A.G., Álvarez, E.Á., Valdés, R.E., Pandal, A., Marigorta, E.B., 2023. Experimental and multiphase modeling of small vertical-axis hydrokinetic turbine with free-surface variations. Renew. Energy 203, 788–801. https://doi.org/10.1016/j.renene.2022.12.114.

Zanforlin, S., Nishino, T., 2016. Fluid dynamic mechanisms of enhanced power generation by closely spaced vertical axis wind turbines. Renew. Energy 99, 1213–1226. https://doi.org/10.1016/j.renene.2016.08.015.

ANSYS FLUENT 12.0 Theory Guide'. Accessed: November. 20, 2023. [Online]. Available: https://www.afs.enea.it/project/neptunius/docs/fluent/html/th/main_pre.htm.

Il Canale Biffis - Claudio Malini - Libro - Sometti - Acque e bonifiche | IBS. https://www.ibs.it/canale-biffis-libro-claudio-malini/e/9788874956760. (Accessed 22 February 2024).